https://doi.org/10.5194/egusphere-2025-5745
Preprint. Discussion started: 15 December 2025

New insights into uncertainties in Antarctic elevation change estimates by comparing radar and laser altimetry

Maria T. Kappelsberger[1], Johan Nilsson[2,3], Martin Horwath[1], Veit Helm[4], and Alex S. Gardner[2]

[1]Chair of Geodetic Earth System Research, TUD Dresden University of Technology, Dresden, Germany
[2]Jet Propulsion Laboratory, California Institute of Technology, Pasadena, USA
[3]Department of Earth Sciences, Uppsala University, Uppsala, Sweden
[4]Alfred-Wegener-Institut Helmholtz-Zentrum für Polar- und Meeresforschung, Bremerhaven, Germany

Correspondence to: Maria T. Kappelsberger (maria.kappelsberger@tu-dresden.de)

Abstract. Satellite radar altimetry has provided continuous observations of Antarctic Ice Sheet (AIS) surface elevation change since 1992. However, uncertainties in radar-derived elevation estimates remain substantial, primarily due to the influence of local surface topography and time-variable signal penetration into snow and firn. The launch of the ICESat-2 laser altimetry mission in late 2018 established a new benchmark for high-accuracy surface elevation measurements, enabling inter-comparison with radar altimetry results and improved assessment of associated uncertainties. In this study, we use the ICESat-2 measurements to evaluate radar altimetry-derived elevation change estimates from CryoSat-2 over the $6\,905\,000\,\mathrm{km}^2$ large and relatively flat interior of the AIS, where topography-related errors are small. We apply a suite of radar-specific correction methods to the CryoSat-2 measurements, including multiple retracking algorithms and empirical corrections for the time-variable surface and volume scattering of the radar signal. We analyse a 5.5-year overlap period between ICESat-2 and CryoSat-2 (April 2019–October 2024) to assess how the different correction methods influence the CryoSat-2 surface elevation change estimates and their uncertainties.

ICESat-2 observations indicate a thickening of $97 \pm 4\,\mathrm{km}^3\,\mathrm{yr}^{-1}$, coinciding with several events of excess snowfall during 2019–2024. All CryoSat-2 solutions yield systematically lower thickening trends, with the smallest bias ($0.6 \pm 1.0\,\mathrm{cm\,yr}^{-1}$ or $42\,\mathrm{km}^3\,\mathrm{yr}^{-1}$) obtained using the AWI-ICENet1 convolutional neural network retracker. The remaining trend differences correlate with the ICESat-2 trend signal itself. We discuss possible causes of these systematic differences, one of which is the hypothesis that temporal variations in radar signal penetration associated to temporal variations in snow properties continue to induce systematic errors in inferred surface elevation changes. If the mean trend difference here were representative of the entire grounded AIS ($12\,352\,700\,\mathrm{km}^2$), it would correspond to an underestimation of AIS volume and mass trends by approximately $74\,\mathrm{km}^3\,\mathrm{yr}^{-1}$ and $28\,\mathrm{Gt\,yr}^{-1}$, respectively. These results underscore the challenges of using radar altimetry to resolve subtle, long-term trends related to surface mass balance changes, while also demonstrating the potential of combined laser-radar altimetry analysis to reduce uncertainties in AIS volume and mass balance estimates.

https://doi.org/10.5194/egusphere-2025-5745
Preprint. Discussion started: 15 December 2025

1 Introduction

Over 1992–2020, the West Antarctic Ice Sheet (WAIS) lost mass at a rate of $82 \pm 9\,\mathrm{Gt\,yr^{-1}}$ according to Otosaka et al. (2023b). The same study reported that, in contrast, the East Antarctic Ice Sheet (EAIS) was close to a state of balance at a rate of $3 \pm 15\,\mathrm{Gt\,yr^{-1}}$. The large mass loss in the WAIS region was mainly due to increased discharge from marine-terminating glaciers as oceanic forcing causes basal melting of ice shelves (Gardner et al., 2018; Hanna et al., 2024). In contrast, the modest EAIS mass gain was mainly influenced by changes in surface mass balance (SMB), specifically increased snowfall due to atmospheric forcing (Smith et al., 2020; Fricker et al., 2025). However, current estimates for the EAIS remain highly uncertain, with conflicting signals on whether it is gaining or losing mass (Nilsson et al., 2022; Otosaka et al., 2023b). Consequently, projections of the EAIS sea-level contribution show a large spread. These range from -7 to $15\,\mathrm{cm}$ by 2100, depending on the compensation of potential ice-dynamical losses from marine-based catchments by SMB (Stokes et al., 2022). Mean annual SMB at the coast is $>500\,\mathrm{kg\,m^{-2}\,yr^{-1}}$ as compared to $<50\,\mathrm{kg\,m^{-2}\,yr^{-1}}$ in the Antarctic Ice Sheet (AIS) interior (Clem et al., 2023). In a warmer climate, SMB is projected to be substantially enhanced over the grounded AIS, including its interior (Kittel et al., 2021; Amory et al., 2024; Ekaykin et al., 2024), where increasing snowfall is expected to be most sensitive to rising temperatures (Nicola et al., 2023). This underscores the need for improved monitoring of the vast interior regions of the AIS to more accurately detect subtle elevation and mass changes.

Since 1992, satellite radar altimeters have continuously measured the surface elevation of the AIS with high spatial resolution (several kilometres), allowing the derivation of temporal elevation changes from local to continent-wide scales (Otosaka et al., 2023a). Between 1992 and 2012, the pulse-limited Ku-Band radar altimetry missions ERS-1, ERS-2 and Envisat mapped the AIS up to about $81.5°$ S (e.g. Wingham et al., 1998; Davis and Ferguson, 2004; Li and Davis, 2008). Unlike these older missions, the ongoing radar mission CryoSat-2 (since 2010) was specially designed to monitor the polar regions and provides measurements up to $88°$ S. Its exact repeat orbit is 369 days with a sub-cycle of 30 days. Over the AIS, CryoSat-2 operates in two different modes: the low resolution mode (LRM) over the interior, and the synthetic aperture radar interferometric mode over the high-relief margins (Wingham et al., 2006). While the latter improves the spatial resolution along track and enables the radar echo to be located more accurately, both of which are needed in complex topography, the former works like a conventional pulse-limited radar system. Even though radar altimetry provides the longest observational record of detailed changes of the AIS (Schröder et al., 2019; Shepherd et al., 2019; Nilsson et al., 2022), limitations in this technique exist. Radar measurements are hampered by a large beam-limited footprint of about $15\,\mathrm{km}$ for CryoSat-2 (ESA, 2021) and by signal penetration into snow and firn (or simply firn hereafter). Over the Antarctic interior, however, topography-related errors and errors due to interpolation effects are small since the ice sheet surface is generally flat and homogeneous (Fig. 1). This allows for the investigation of errors related to radar signal penetration and the methods used to mitigate them: waveform retracking and scattering correction, which will be detailed below.

The radar return signal (the waveform) is formed from a combination of surface and volume scattering (Ridley and Partington, 1988; Legrésy and Rémy, 1997; Larue et al., 2021; Helm et al., 2024). Surface scattering is controlled by local height undulations and surface roughness down to centimetre scale. Volume scattering is affected by the firn properties, such as grain

https://doi.org/10.5194/egusphere-2025-5745
Preprint. Discussion started: 15 December 2025

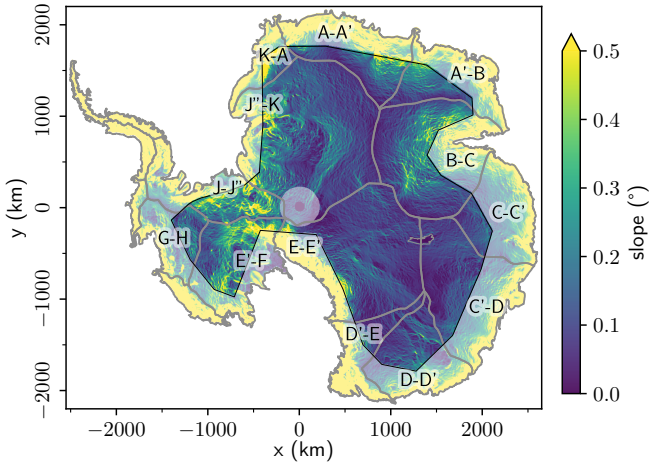

Figure 1. The ice surface slope derived from the Reference Elevation Model of Antarctica (Howat et al., 2019, 2022). Thick grey lines indicate the ice grounding line and drainage basin outlines as defined by Rignot et al. (2011a, b). Drainage basins are labelled if they extend into our study area, which is the highlighted low resolution mode (LRM) zone of CryoSat-2. A thin grey line shows the shoreline of subglacial Lake Vostok (Popov and Chernoglazov, 2011), located at the border of basins E-E' and C'-D.

size and temperature, and varies strongly over space and time. Retracking algorithms define a point on the leading edge of the waveform to be representative of the ice sheet elevation at the surface (e.g. Bamber, 1994). The choice of the retracker is crucial for suppressing elevation biases (Schröder et al., 2017). However, elevations retrieved from conventional retracking methods can still be biased by around 21 cm over the EAIS plateau (Larue et al., 2021) and their temporal evolution can remain with spurious large variations due to changes in firn properties (Helm et al., 2024). For this reason, retracked elevation changes typically require an empirical correction for the time-variable surface and volume scattering, referred to as scattering correction. This correction further reduces artificial elevation changes by exploiting their correlation with variations in waveform parameters (e.g. Davis and Ferguson, 2004; Flament and Rémy, 2012; Simonsen and Sørensen, 2017). For example, uncorrected CryoSat-2 elevation changes over Lake Vostok would suggest a trend of $1.3 \pm 0.4\,\mathrm{cm\,yr^{-1}}$ for 2011–2019, whereas applying a scattering correction yields a more realistic estimate of $0.3 \pm 0.2\,\mathrm{cm\,yr^{-1}}$ (Fig. 2 in Nilsson et al., 2022). Moreover, the standard deviation (SD) of detrended elevation change time series decreased by 4 to 10 cm according to Helm et al. (2024) when applying the scattering correction to conventionally retracked measurements over the EAIS plateau.

ICESat-2 (since 2018) is the first continuously measuring laser altimetry mission, using green laser pulses (532 nm) split into three beam pairs (Markus et al., 2017). It has an exact repeat orbit of 91 days with a monthly sub-cycle for the polar regions. ICESat-2 provides measurements of higher accuracy and along-track resolution than radar altimetry and is ideal for observing elevation changes of the AIS as its green laser virtually has no penetration into the firn layer (Studinger et al., 2024) and its small footprint of 11 m (Magruder et al., 2021). Brunt et al. (2021) assessed the ICESat-2 heights based on comparisons with GNSS data over the flat EAIS interior (along latitude 88° S), finding biases of <3.3 cm and precisions of <7.2 cm. The largest source of error in laser altimetry is geolocation errors due to systematic pointing errors and their temporal variation.

https://doi.org/10.5194/egusphere-2025-5745
Preprint. Discussion started: 15 December 2025

These errors are largely calibrated and corrected for by the ICESat-2 ground processing and fulfil the mission requirements (Bae et al., 2021; Luthcke et al., 2021). Using corner cube retro-reflectors, Magruder et al. (2021) found a mean geolocation accuracy of $3.4 \pm 2.5\,\mathrm{m}$ over the area along 88° S. Comparing global sea-level trends between ICESat-2 and radar altimetry data over a period of $3.5\,\mathrm{yr}$ revealed an ICESat-2 long-term drift of $<2\,\mathrm{mm\,yr^{-1}}$ (Magruder et al., 2025). Thus far, it is not expected that this error will be significantly higher over ice sheets than over the ocean; therefore, an accuracy of $<2\,\mathrm{mm\,yr^{-1}}$ for ICESat-2 trends in AIS elevation change can be anticipated (Magruder et al., 2025).

The unprecedented accuracy of ICESat-2 measurements provides a new opportunity to validate radar altimetry results across vast overlapping areas. This is a significant advantage over local GNSS comparisons and limited airborne validation campaigns. Previous studies have used data from ICESat-2 and radar altimetry to derive surface elevation changes of the AIS (Li et al., 2022; Nilsson et al., 2022; Yue et al., 2023). However, these studies did not focus on a detailed comparison between the radar and laser results. For the Greenland Ice Sheet, Ravinder et al. (2024) investigated results from ICESat-2 and CryoSat-2 over the period 2018–2022. Using their optimal elevation change solutions, they stated a mean difference in trend of $-0.3 \pm 1.8\,\mathrm{cm\,yr^{-1}}$ (ICESat-2−CryoSat-2). Helm et al. (2024) published a novel radar retracking algorithm applied to CryoSat-2 LRM measurements in Greenland and Antarctica. They validated their CryoSat-2 results by ICESat-2 trends over the period 2019–2021 and stated differences of $<1\,\mathrm{cm\,yr^{-1}}$. Nevertheless, more work is required to better understand the differences between ICESat-2 and CryoSat-2 results, since these differences directly affect mass balance estimates. This applies in particular to the Antarctic interior as changes are subtle and dominated by surface processes.

The uncertainty in EAIS mass trends derived from altimetry has previously been stated at about 5 to $6\,\mathrm{Gt\,yr^{-1}}$ (Shepherd et al., 2019, for 1992–2017; Schröder et al., 2019, for 1992–2017; Fig. 3a in Otosaka et al., 2023b, for 2003–2019). This uncertainty requires an uncertainty of the spatial mean of elevation change trends at $2\,\mathrm{mm\,yr^{-1}}$ or smaller, depending on the density assumed (snow to ice). The underlying uncertainty assessments are limited by an insufficient understanding of all sources of uncertainty and their stochastic characteristics. This is because long-term altimetric mass balance estimates are affected by various spatially and temporally correlated errors, such as errors related to the surface topography, time-variable radar signal penetration, volume-to-mass conversion and intermission calibration. Improved understanding of laser–radar differences can help enhance the characterisation of the uncertainty in altimetric estimates.

In this study, we analyse coincident CryoSat-2 (2010–2024) and ICESat-2 (2019–2024) measurements over the CryoSat-2 LRM zone of Antarctica. This region encompasses $6\,905\,000\,\mathrm{km^2}$ of the relatively flat interior of the AIS and provides an ideal test area for inter-mission comparison. Our primary goal is to improve the understanding of uncertainties in AIS volume and mass balance estimates by quantifying how CryoSat-2 and ICESat-2 elevation change results diverge under different processing regimes. To achieve this, we apply a suite of state-of-the-art CryoSat-2 correction methods designed to mitigate the effects of radar signal penetration and surface and volume scattering. The methods include different conventional retracking algorithms and one neural network–based retracker, as well as several formulations of time-variable scattering corrections. We evaluate how these methods influence the detection of surface elevation changes and the corresponding uncertainty estimates, both spatially and temporally. Uncertainties are quantified using internal consistency tests and external validation against coincident ICESat-2 results. Through this analysis, we address three overarching questions:

https://doi.org/10.5194/egusphere-2025-5745
Preprint. Discussion started: 15 December 2025

- Which of the radar-specific correction methods, particularly retracking and scattering corrections, yield the most accurate surface elevation change estimates when validated with ICESat-2?
- How consistent are CryoSat-2 and ICESat-2 elevation change trends across their 5.5-year period of overlap?
- What level of certainty or accuracy can currently be achieved in determining elevation changes of the vast, low-relief AIS interior?

Together, these questions guide our assessment of how radar-specific uncertainties propagate into large-scale AIS volume and mass balance estimates, and how the integration of radar and laser altimetry can help constrain them.

2 Altimetry elevation measurements

2.1 ICESat-2 laser altimetry

We use the ICESat-2 ATL06 land ice height product Version 6 from the National Snow and Ice Data Center (Smith et al., 2023). ATL06 provides surface elevations (heights above the WGS84 ellipsoid, ITRF2014 reference frame) in 40 m segments every 20 m and is derived from the ATL03 global geolocated photon data (Smith et al., 2019). To reduce the large data amount, we only take into account every tenth measurement. ATL03 provides surface elevations of the individual photons corrected for the atmospheric propagation delay, the solid Earth tides, pole tides and ocean loading tides. Since Version 6, a time and temperature dependent range bias correction from onboard calibration data is included for ATL03 (Neumann et al., 2022). ATL06 further corrects for the transmit-pulse shape bias and the first photon (i.e. saturation) bias (Smith et al., 2019).

We use the ATL06 elevations over the period April 2019 to October 2024 from all six beams. Measurements prior to April 2019 (cycles 1 and 2) are excluded as they show an unknown spread, possibly because ICESat-2 was not pointing at the reference ground track during this early mission phase (Luthcke et al., 2021). Moreover, measurements during May and June 2024 are not considered due to large data gaps resulting from a solar storm. For data editing, we follow the procedure of Smith et al. (2020), which excludes height measurements (a) $>10\,000$ m that result from atmospheric scattering, (b) of poor quality as determined by the quality summary parameter included in the product, and (c) having a difference of >2 m between consecutive points long-track (20 m spacing), taking into account the surface slope between the two points. We note that we refrain from using the higher-level ATL15 product of gridded elevation changes in order to enable consistent processing of the ICESat-2 and CryoSat-2 data. This allows for greater flexibility when comparing the two datasets and avoids us being restricted by the three-month temporal resolution of the ATL15 product.

2.2 CryoSat-2 radar altimetry from three conventional retrackers

We make use of the European Space Agency (ESA) CryoSat-2 Baseline E Level 1B (L1B) and Level 2 In-depth (L2I) products (ESA, 2023a, b). While L1B provides the complete waveform information, L2I offers fully corrected surface elevations (heights above the WGS84 ellipsoid, ITRF2014 reference frame). Both data are given at a sampling rate of 20 Hz, equating to approximately 370 m along the track. The effective resolution is about 1.65 km, which is the width of the pulse-limited

https://doi.org/10.5194/egusphere-2025-5745
Preprint. Discussion started: 15 December 2025

footprint (ESA, 2021). We use the L1B and L2I data over November 2010 to November 2024. Data prior to November 2010 are excluded due to low availability of measurements. Height measurements of poor quality are excluded using the height error flag included in the product.

The L2I elevations are ready-to-use and widely applied for land ice applications (e.g. Slater et al., 2018; Sandberg Sørensen et al., 2018; Otosaka et al., 2019; Zhang et al., 2020; Hai et al., 2022; Li et al., 2022). They are corrected for instrument effects, atmospheric propagation delays, tidal effects (ocean loading, solid Earth and pole tides) and the surface slope within the beam-limited footprint. For the latter, called slope correction, the height measurements are relocated from nadir to the echo position up-slope using the digital elevation model of Helm et al. (2014). The L2I product provides solutions from two different retrackers over land ice in LRM, which we both incorporate: the University College London land ice (UCL-LI) retracker, also known as Ice-2 (Legrésy et al., 2005); and the offset center of gravity (OCOG) retracker (Wingham et al., 1986; Bamber, 1994), also known as Ice-1. The UCL-LI retracker is a functional fit retracker based on fitting a Brown (1977) model, adapted for CryoSat-2, to the waveform. The OCOG retracker is a threshold retracker and the ESA L2I results refer to $30\,\%$ of the OCOG amplitude (ESA EO Help, personal communication, 29 April 2025). For further details on both retracking algorithms the reader is referred to Ronan et al. (2024).

We independently analyse the L1B waveforms, corrected for instrument effects, in order to apply an in-house retracking algorithm. We use the OCOG algorithm, where, unlike ESA's L2I solution, we apply a lower threshold. Following Schröder et al. (2019), we define $10\,\%$ of the OCOG amplitude as the surface elevation, since it is known that using a lower threshold reduces the sensitivity to time-variable firn properties and results in more precise elevation change estimates (e.g. Davis, 1997; Schröder et al., 2019). This approach was also applied by Krieger et al. (2020) and Kappelsberger et al. (2024), and is similar to other low-threshold retrackers, such as those used by Nilsson et al. (2022) and for the ESA land ice product of the CryoTEMPO project (Andersen, 2025; Muir, 2024). We correct the retracked elevations for atmospheric propagation delays and tidal effects as suggested in the CryoSat-2 Product Handbook (ESA, 2021). Further, we apply a slope correction based on the relocation method (Roemer et al., 2007; Schröder et al., 2019), using the same digital elevation model employed in the processing of ESA L2I products. To distinguish the two OCOG retracking solutions, we refer to them as OCOG30 and OCOG10 for the ESA L2I and our own processing, respectively.

3 Methods of deriving monthly gridded elevation changes

3.1 Removing the static topography

To derive time-variable elevation changes of the ice surface, we subtract the static topography from each measurement of absolute elevation. The static topography is estimated by fitting a topography model for every prediction point to all height measurements (h_i) within a $1\,\mathrm{km}$ search radius, provided that at least five observations are available and they span a time period of at least $2.5\,\mathrm{yr}$. The location of the prediction points is not fixed, but iteratively shifted as done by Nilsson et al. (2022). Our initial prediction points are $1\,\mathrm{km}$ spaced grid cell centres in polar stereographic projection. From all locations of h_i (x_i and y_i), we calculate the median location (x^{m} and y^{m}) and use it as a new prediction point in the next iteration (maximum of two). In

https://doi.org/10.5194/egusphere-2025-5745
Preprint. Discussion started: 15 December 2025

this way, our prediction points follow the satellite ground tracks, taking into account the orbital configuration of each mission, which is especially important for ICESat-2 due to its reference track geometry.

We fit a different topography model to h_i depending on the number of observations (Nilsson et al., 2022). If less than sixteen but more than 5 observations are available, we use a bilinear model. For each iteratively defined prediction point, it reads

$$\begin{aligned} h_i &= p\,\mathrm{d}t_i + a_0 + a_1\,\mathrm{d}x_i + a_2\,\mathrm{d}y_i + \epsilon_i \\ &= p\,\mathrm{d}t_i + h_i^{\mathrm{topo}} + \epsilon_i, \end{aligned} \tag{1}$$

with $\mathrm{d}t_i = t_i - t^{\mathrm{m}}$, $\mathrm{d}x_i = x_i - x^{\mathrm{m}}$ and $\mathrm{d}y_i = y_i - y^{\mathrm{m}}$. Thereby, t_i is the time of the measurement and t^{m} the middle of the full mission period considered, which is 15 November 2017 for CryoSat-2 and 15 January 2022 for ICESat-2. The linear trend p is estimated with reference to t^{m}. The residuals are denoted by ϵ_i. If more than fifteen observations are available, we use a bi-quadratic model. For each iteratively defined prediction point, it reads

$$\begin{aligned} h_i &= p\,\mathrm{d}t_i + a_0 + a_1\,\mathrm{d}x_i + a_2\,\mathrm{d}y_i \\ &\quad + a_3\,\mathrm{d}x_i^2 + a_4\,\mathrm{d}y_i^2 + a_5\,\mathrm{d}x_i\,\mathrm{d}y_i + \epsilon_i \\ &= p\,\mathrm{d}t_i + h_i^{\mathrm{topo}} + \epsilon_i. \end{aligned} \tag{2}$$

We solve for the linear trend p and the three or six topography parameters ($a_0 ... a_2$ or $a_0 ... a_5$) using an iterative least-squares adjustment in order to remove outliers from the data. After each iteration (maximum of five), those observations are excluded whose associated absolute values of the residuals exceed 3 times the median absolute deviation (MAD) of all residuals within the search area. Moreover, solutions are rejected if the estimated trend p is $>20\,\mathrm{m\,yr^{-1}}$. To infer the elevation changes over time ($\mathrm{d}h_i$), the estimated static topography is subtracted from the non-rejected heights for each prediction point according to

$$\mathrm{d}h_i = h_i - h_i^{\mathrm{topo}} = p\,\mathrm{d}t_i + \epsilon_i. \tag{3}$$

Those elevation changes $\mathrm{d}h_i$ are rejected whose absolute values are $>10\,\mathrm{m}$. To derive one estimate of elevation change per month that is representative of the prediction point at x^{m} and y^{m}, we calculate the mean and SD (denoted by $\mathrm{d}h^{\mathrm{m}}$ and $\sigma_{\mathrm{d}h^{\mathrm{m}}}$, respectively) of all $\mathrm{d}h_i$ within that month. We exclude those $\mathrm{d}h_i$ whose absolute difference to $\mathrm{d}h^{\mathrm{m}}$ exceeds 3 times $\sigma_{\mathrm{d}h^{\mathrm{m}}}$. We note that $\mathrm{d}h^{\mathrm{m}}$ and $\sigma_{\mathrm{d}h^{\mathrm{m}}}$ refer to the reference time t^{m}, which is the middle of the mission period. Therefore, $\sigma_{\mathrm{d}h^{\mathrm{m}}}$ tends to be largest at the start and end of the mission period.

We apply this algorithms individually to the ICESat-2 heights and the three different CryoSat-2 height solutions (OCOG10, OCOG30, UCL-LI). To account for a potential bias between ascending (A) and descending (D) tracks (A–D bias) (Legresy et al., 1999; Remy et al., 2006; Arthern et al., 2001; Armitage et al., 2014), we further process the heights from A and D tracks separately. In total, we generate eight $\mathrm{d}h^{\mathrm{m}}$ results.

3.2 Filtering and interpolation

Before using the $\mathrm{d}h^{\mathrm{m}}$ results to derive a homogeneous and complete grid of elevation changes, we clean the data using a spatial outlier filter. For each month, we group $\mathrm{d}h^{\mathrm{m}}$ into $50\,\mathrm{km} \times 50\,\mathrm{km}$ tiles and calculate the local median and MAD for each tile.

https://doi.org/10.5194/egusphere-2025-5745
Preprint. Discussion started: 15 December 2025

Values are rejected if their deviation from the median exceed $0.5\,\mathrm{m}$ plus 3 times the MAD. We follow Schröder et al. (2019) by adding $0.5\,\mathrm{m}$ to the outlier criterion to prevent small elevation variations with a low regional MAD from being classified as outliers.

We smooth and interpolate the cleaned $\mathrm{d}h^{\mathrm{m}}$ results onto a regular grid of $5\,\mathrm{km}$ spacing using a Gaussian kernel. The interpolation is performed for every monthly $\mathrm{d}h^{\mathrm{m}}$ slice individually. We estimate the elevation change $\mathrm{d}h$ for every month at every grid point according to

$$\mathrm{d}h = \frac{\sum(w_j\,\mathrm{d}h_j^{\mathrm{m}})}{\sum w_j}, \tag{4}$$

with the weights w_j defined as

$$w_j = \frac{1}{\sigma^2_{\mathrm{d}h_j^{\mathrm{m}}}} \exp\frac{-d_j^2}{2\alpha^2}. \tag{5}$$

The weights follow a Gaussian function with $\alpha = 20\,\mathrm{km}$. They not only consider the distances d_j between the location of the grid point and $\mathrm{d}h_j^{\mathrm{m}}$ but also the uncertainties $\sigma_{\mathrm{d}h_j^{\mathrm{m}}}$, which are comparable within each month over space. We use the 30 closest $\mathrm{d}h^{\mathrm{m}}$ estimates within each of four quadrants around the grid point and within a maximum search radius of $50\,\mathrm{km}$.

We calculate the uncertainty of the interpolated elevation changes ($\sigma_{\mathrm{d}h}$) following Schröder et al. (2019), combining the interpolation error and an average error according to

$$\sigma^2_{\mathrm{d}h} = \frac{\sum(w_j\,(\mathrm{d}h - \mathrm{d}h_j^{\mathrm{m}})^2)}{\sum w_j} + \mathrm{median}(\sigma^2_{\mathrm{d}h_j^{\mathrm{m}}}). \tag{6}$$

After the filtering and interpolation in the spatial domain, a final outlier filter is applied in the temporal domain. For each grid cell, we calculate the MAD of the detrended time series of $\mathrm{d}h$ and remove values in $\mathrm{d}h$ where the detrended time series exceeds 5 times the MAD. The rejected values and missing values (in case no data are available within the $50\,\mathrm{km}$ search radius) are filled using a third order spline interpolation. Their uncertainties are set to the uncertainty time series' maxima.

As for the derivation of $\mathrm{d}h^{\mathrm{m}}$, the interpolation and filtering is implemented individually for the ICESat-2, CryoSat-2 OCOG10, OCOG30 and UCL-LI estimates from A and D tracks.

3.3 Scattering correction for CryoSat-2 from four approaches

We empirically correct the elevation changes ($\mathrm{d}h$) from CryoSat-2 (OCOG10, OCOG30, UCL-LI) for time-variable surface and volume scattering using the correlation between $\mathrm{d}h$ and variations in the waveform parameters. We do this separately for A and D tracks. In contrast to previous studies that implemented the scattering correction and the estimation of a topography model within a single multi-parameter regression (e.g. Simonsen and Sørensen, 2017; Sandberg Sørensen et al., 2018; Schröder et al., 2019), we separate these two steps following Nilsson et al. (2022). This allows for a more tailored regression for each step. Here, we implement the scattering correction on the basis of monthly interpolated grids instead of single point-based measurements since this minimizes the sensitivity to individual waveform outliers and increases the correlation between $\mathrm{d}h$ and the waveform parameters (Helm et al., 2024).

https://doi.org/10.5194/egusphere-2025-5745
Preprint. Discussion started: 15 December 2025

Table 1. The four different approaches to scattering correction applied to the CryoSat-2 solutions from the OCOG10, OCOG30 and UCL-LI retrackers.

Suffix to the retracker name	Waveform parameter	Time series preprocessing
a	BS	centring (Eq. 7)
b	LEW	centring (Eq. 8)
c	BS, LEW	centring (Eq. 9)
d	BS, LEW	differencing (Eq. 10)

The waveform parameters backscatter (BS), leading edge width (LEW) and trailing edge slope are typically used to describe the shape of the waveform (Legrésy and Rémy, 1998; Legrésy et al., 2005). Here, we include the BS and LEW. The trailing edge slope is not considered because it is not well correlated with dh. We use the BS estimate of the OCOG amplitude provided by the ESA L2I product and we obtain the LEW from the difference of the times at $50\,\%$ and $10\,\%$ of the OCOG amplitude scaled by 2.5 (Krieger et al., 2020). We apply the same processing scheme to the waveform parameters as to the height measurements h_i, just without fitting a trend and topography model (i.e., without applying Eqs. 1–3). Thus, the derivation of monthly mean BS and LEW estimates and their interpolation and filtering are performed separately for A and D tracks to account for A–D biases, which are also present in the waveform parameters (Remy et al., 2006; Rémy et al., 2012).

The scattering correction can be computed and applied in various ways. Here, we apply four different configurations from the literature (Table 1). These approaches are implemented individually for each $5\,\mathrm{km}$ grid cell of the six CryoSat-2 dh solutions (three retrackers for each of the A and D tracks) using least-squares adjustment. First, we solely use the BS (e.g. McMillan et al., 2014; Schröder et al., 2019; Zhang et al., 2020) and estimate the gradient G^{BS} of the centred BS time series as

$$\mathrm{d}h_k = G^{\mathrm{BS}} \cdot (\mathrm{BS}_k - \overline{\mathrm{BS}}) + \epsilon_k, \tag{7}$$

where $k = 1...169$ refers to the months from November 2010 to November 2024 and the overbar denotes the mean value of the time series. We refer to this as correction a. Second, we solely use the LEW (e.g. Sandberg Sørensen et al., 2018; Krieger et al., 2020) and estimate the gradient G^{LEW} of the centred LEW time series as

$$\mathrm{d}h_k = G^{\mathrm{LEW}} \cdot (\mathrm{LEW}_k - \overline{\mathrm{LEW}}) + \epsilon_k. \tag{8}$$

We refer to this as correction b. Third, we incorporate both the BS and LEW (e.g. Li et al., 2022; Helm et al., 2024) and estimate the gradients G^{BS} and G^{LEW} of the centred BS and LEW time series as

$$\mathrm{d}h_k = G^{\mathrm{BS}} \cdot (\mathrm{BS}_k - \overline{\mathrm{BS}}) + G^{\mathrm{LEW}} \cdot (\mathrm{LEW}_k - \overline{\mathrm{LEW}}) + \epsilon_k. \tag{9}$$

We refer to this as correction c. Fourth, we apply a difference operator to the time series, i.e. we calculate the difference between consecutive months (e.g. Khvorostovsky, 2012; Nilsson et al., 2022), and then smooth the time series using a Savitzky–Golay filter with a window length of seven months. We use the resulting smoothed, differenced time series (Δdh, ΔBS, ΔLEW) to

https://doi.org/10.5194/egusphere-2025-5745
Preprint. Discussion started: 15 December 2025

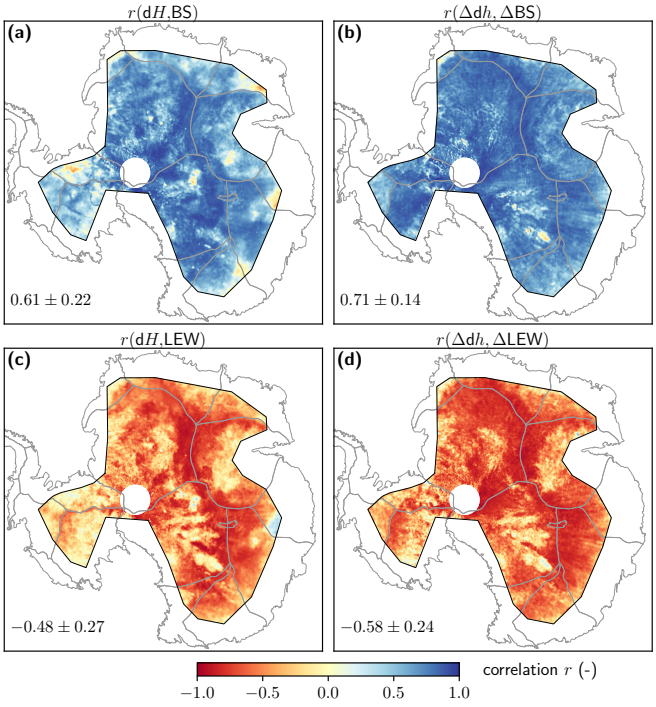

Figure 2. Correlation r between temporal variations of elevation (dh) and temporal variations of the waveform parameter (a, b) backscatter (BS) and (c, d) leading edge width (LEW). The temporal variations are expressed either by (a, c) the centred time series (dh, BS, LEW), or by (b, d) differencing the time series (Δdh, ΔBS, ΔLEW). Results are shown for the OCOG10 retracker and all ascending tracks. The mean $\pm$ SD for the entire LRM zone are stated in the lower left corner. Here and in the following maps, the SD is calculated as 1.253 times the mean absolute deviation to ensure robustness against outliers.

focus on short-term variations, thereby increasing the correlation between the time series (Fig. 2). We estimate the gradients G^{BS} and G^{LEW} as

$$\Delta \mathrm{d}h_k = G^{\mathrm{BS}} \cdot \Delta \mathrm{BS}_k + G^{\mathrm{LEW}} \cdot \Delta \mathrm{LEW}_k + \epsilon_k. \tag{10}$$

We refer to this as correction d. We tested another scattering correction approach that focuses on short-term variations by correlating the time series over shorter intervals and estimating time-variable gradients (e.g. Khvorostovsky, 2012; Shepherd et al., 2019). However, we refrain from introducing this approach, since applying it in addition to time series differencing generates results that hardly differ from those obtained by using correction d alone. While these differences are marginal overall, we acknowledge that localised differences may still exist. Additionally, using centred time series may increase sensitivity to the chosen time interval.

To derive the corrected elevation changes (dh^{cor}), the estimated gradients G^{BS} and G^{LEW} are applied to the dh time series according to the general form

$$\mathrm{d}h_k^{\mathrm{cor}} = \mathrm{d}h_k - [G^{\mathrm{BS}} \cdot (\mathrm{BS}_k - \overline{\mathrm{BS}}) + G^{\mathrm{LEW}} \cdot (\mathrm{LEW}_k - \overline{\mathrm{LEW}})]. \tag{11}$$

https://doi.org/10.5194/egusphere-2025-5745
Preprint. Discussion started: 15 December 2025

For correction c and d (Eqs. 9 and 10), the general form of Eq. (11) applies exactly. For corrections a and b (Eqs. 7 and 8), only the first and second summand, respectively, remain in the term in square brackets in Eq. (11).

3.4 Combining results from ascending and descending tracks

The altimetry processing methods described in Sects. 3.1–3.3 are applied to A and D tracks separately. In this step, we combine these two individual solutions. We derive the final grids of monthly surface elevation changes by calculating the weighted mean of the two elevation change solutions from both tracks for each grid cell and each month. The corresponding elevation change uncertainties from both tracks (σ_{dh}) are used for weighting.

Ultimately, we derive one result and 15 different results of monthly gridded elevation changes for the Antarctic interior from ICESat-2 and CryoSat-2, respectively. For CryoSat-2, we obtained solutions from three retrackers (OCOG10, OCOG30, UCL-LI) without applying any scattering correction, and with the four corrections (a–d; Table 1) applied to each retracker solution. When a correction is applied, the relevant label (a, b, c or d) is added to the end of the retracker's name. For example, the CryoSat-2 elevation change results from the retracker OCOG10 and the scattering correction using monthly differences of both BS and LEW is referred to as OCOG10d.

4 Additional data products

4.1 CryoSat-2 elevation changes from the AWI-ICENet1 retracker

In addition to the 15 CryoSat-2 results from our analysis using conventional retracking algorithms (Sect. 2 and 3), we include an update of the CryoSat-2 results from Helm et al. (2024). That study designed a novel retracker called AWI-ICENet1 which is based on a deep convolutional neural network architecture. This network was trained with 3.8 million simulated waveforms that considered different topographies, surface slopes and attenuations, and was then applied to the CryoSat-2 waveforms in LRM. Compared to the elevation change solutions derived from conventional retrackers, the AWI-ICENet1 retracker achieves lower uncertainties due to a large reduction in time-variable radar signal penetration (Helm et al., 2024).

Helm et al. (2024) provide four different results of monthly gridded surface elevation changes based on their AWI-ICENet1 retracker at a spatial resolution of 5 km. The first result is given without applying any scattering correction algorithm. The other three results are obtained by applying a scattering correction using either the BS time series alone, the LEW time series alone, or both the BS and LEW time series. As these three corrections are similar to the corrections a–c described in Sect. 3.3, we use the same naming convention and refer to them as AWI-ICENet1a, AWI-ICENet1b and AWI-ICENet1c.

4.2 Firn height changes from the GEMB model

We incorporate elevation changes of the Antarctic firn column due to SMB changes and firn air content (FAC) evolution from the Glacier Energy and Mass Balance (GEMB) model (Gardner et al., 2023). GEMB is a vertical column model and simulates the ice sheet and glacier surface atmospheric mass and energy exchange and the evolution of the firn state. Processes such

https://doi.org/10.5194/egusphere-2025-5745
Preprint. Discussion started: 15 December 2025

Table 2. Metrics used for assessing the various altimetry datasets.

Symbol	Name	Calculation based on	Unit
σ_{AD}	precision	altimetry A−D times series (Sect. 5.1)	m
σ_{IC}	accuracy	ICESat-2−CryoSat-2 time series (Sect. 5.1)	m
σ_0	noise level	altimetry−GEMB time series (Sect. 5.2.1)	m
κ	spectral index	noise's power spectral density (Sect. 5.2.1)	unitless
$\sigma_{\dot{\mathrm{d}}h}$	trend uncertainty	σ_0 and κ (Eq. 12, Sect. 5.2.1)	$\mathrm{m\,yr^{-1}}$
$\delta\dot{\mathrm{d}}h$	trend error	ICESat-2−CryoSat-2 trend (Sect. 5.2.2)	$\mathrm{m\,yr^{-1}}$
$\sigma_{\delta\dot{\mathrm{d}}h}$	trend error uncertainty	ICESat-2 and CryoSat-2 $\sigma_{\dot{\mathrm{d}}h}$ (Sect. 5.2.2)	$\mathrm{m\,yr^{-1}}$

as snow grain size evolution, thermal diffusion, meltwater retention, percolation, refreezing, runoff, and firn densification are considered (Gardner et al., 2023). The SMB is based on an atmospheric forcing of 3-hourly, $31\,\mathrm{km}\times31\,\mathrm{km}$ spatially resolved ERA5 reanalysis data (Hersbach et al., 2020), namely precipitation, air temperature, wind speed, water vapor and surface pressure, downwelling longwave and shortwave radiation, and is given in units of metre ice equivalent.

The outputs are available monthly on a $10\,\mathrm{km}$ grid from January 1979 to December 2024 (Schlegel and Gardner, 2025). Cumulative SMB anomalies are derived with respect to the 1979–2009 climatology, as done by Gardner et al. (2023), and are summed with the height changes of FAC. This gives us modelled AIS elevation changes due to SMB and firn processes, with the assumption that rates of solid-ice divergence match the 1979–2009 SMB climatology. Finally, we interpolate the firn height changes onto a $5\,\mathrm{km}$ grid to be consistent with the altimetry results.

5 Methods of assessing altimetry results

We thoroughly assess the uncertainties in our ensemble of altimetry results. The metrics listed in Table 2 are used to assess uncertainty from different perspectives, as explained in the following sections.

5.1 Precision and accuracy

We assess the precision (i.e. the repeatability) of each of the 19 altimetry datasets derived in this study (Sect. 2 and 3) at the grid-cell level. We calculate the temporal root mean square (RMS) of the difference time series in elevation change between the A and D track solutions for each dataset and grid cell. This metric is denoted as σ_{AD}.

We assess the accuracy of each of the 15 CryoSat-2 datasets derived in this study as well as of the four CryoSat-2 datasets based on the AWI-ICENet1 retracker (Sect. 4.1) by comparing them with the ICESat-2 result. Since we consider the ICESat-2 elevation changes to be the estimates closest to the truth (i.e. the most accurate estimates), we assume them to be reasonable for validating CryoSat-2 results. The CryoSat-2 accuracy is calculated as the temporal RMS of the difference time series in elevation change between ICESat-2 and CryoSat-2. This metric is denoted as σ_{IC}.

https://doi.org/10.5194/egusphere-2025-5745
Preprint. Discussion started: 15 December 2025

5.2 Trend analysis

For the overlapping time period of CryoSat-2 and ICESat-2 data (April 2019–October 2024), we fit a linear trend ($\mathrm{d}\dot{h}$) to the elevation change time series using ordinary least-squares regression. The trend is adjusted for each grid cell of each of the 20 altimetry datasets individually. For comparison, we also fit a trend to the GEMB firn height changes.

5.2.1 Trend uncertainty

Due to real signals, primarily SMB variations and time-variable firn processes, as well as altimetry errors resulting from these processes, such as time-variable radar signal penetration, altimetry time series over ice sheets exhibit temporal correlation (Ferguson et al., 2004; King and Watson, 2020; Kappelsberger et al., 2024). Ignoring temporal correlations, that is assuming white noise, leads to a significant underestimation of the trend uncertainty (King and Watson, 2020; King and Christoffersen, 2024).

To quantify the impact of correlated noise on our trend uncertainty estimate, we analyse the stochastic properties of the altimetry noise (ϵ) for each individual time series of each dataset. We define noise as anything that cannot be explained by changes in firn height (using the GEMB model), which cause large seasonal and interannual variations, or by a linear trend. For each grid cell, we calculate the power spectral density of ϵ and estimate its spectral index (κ) for power-law noise by fitting a line to the power spectral density in log-log space (Bos et al., 2020). The slope of the line corresponds to κ, reflecting the degree of temporal correlation (e.g. $\kappa = 0$ for white noise, $\kappa = -1$ for flicker noise). Figures S1 and S2 demonstrate this procedure by showing time series of ϵ and their power spectral density for two selected grid cells. The estimated value of κ (maximum of 0) is used to construct the full covariance matrix describing the stochastic properties of ϵ (Bos et al., 2020).

To assess the standard uncertainty of the trend ($\sigma_{\mathrm{d}\dot{h}}$) for each grid cell and dataset, we propagate the associated correlated noise characteristics using

$$\sigma^2_{\mathrm{d}\dot{h}} = \sigma^2_0 \cdot \mathrm{diag}[(\mathbf{A^T P A})^{-1}], \tag{12}$$

where $\mathbf{A}$ is the design matrix containing the derivatives after $\mathrm{d}\dot{h}$, $\mathbf{P}$ is the weight matrix resulting from the inverse of the covariance matrix, and σ^2_0 is the variance of unit weight representing the noise level. The estimate of σ^2_0 is derived by dividing the weighted variance of the noise ($\epsilon^T \mathbf{P} \epsilon$) by the system's redundancy (e.g. Koch, 1999). Thus, a larger (more positive) σ_0, but also a smaller (more negative) κ (i.e. a higher temporal correlation) increase the estimate of $\sigma_{\mathrm{d}\dot{h}}$.

5.2.2 CryoSat-2 trend error

We validate the 19 different CryoSat-2 trend estimates (15 from our study and four from AWI) by comparing them with the ICESat-2 trend estimate at grid cell level. The difference in trends (ICESat-2 minus CryoSat-2) is denoted $\delta\mathrm{d}\dot{h}$. Assuming the ICESat-2 trend to be the closest to the truth, $\delta\mathrm{d}\dot{h}$ can be considered the true trend error in the associated radar analysis method. The corresponding standard uncertainty estimate ($\sigma_{\delta\mathrm{d}\dot{h}}$) is derived by propagating the trend uncertainties ($\sigma_{\mathrm{d}\dot{h}}$) of ICESat-2 and the associated CryoSat-2 dataset, which describes the stochastic characteristics of $\delta\mathrm{d}\dot{h}$.

https://doi.org/10.5194/egusphere-2025-5745
Preprint. Discussion started: 15 December 2025

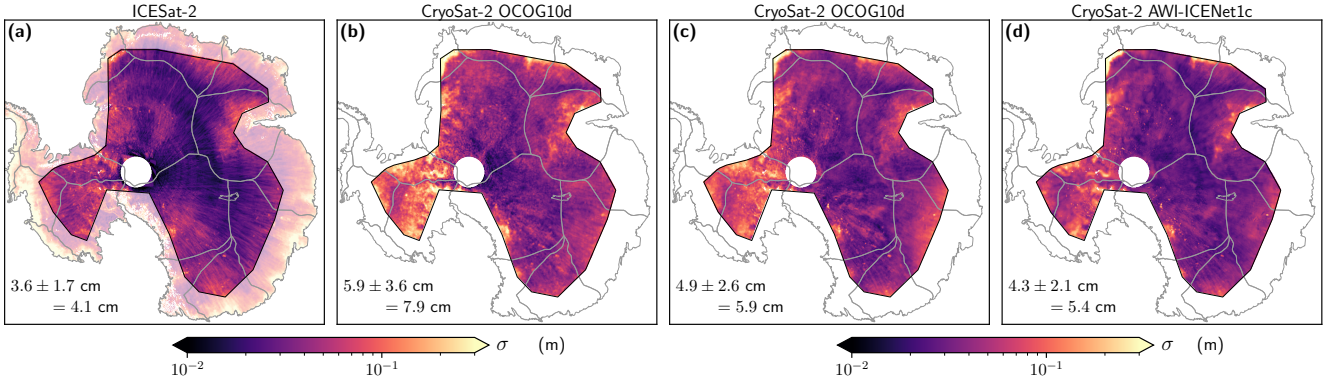

Figure 3. (a, b) Precision (σ_{AD}) from ascending minus descending results for (a) ICESat-2 and (b) CryoSat-2 OCOG10d. (c, d) CryoSat-2 accuracy (σ_{IC}) from ICESat-2 minus CryoSat-2 time series for (c) OCOG10d and (d) AWI-ICENet1c. The mean ± SD and RMS for the entire LRM zone are stated in the lower left corner.

5.2.3 Area-wide estimates

We calculate trends in volume change ($\Sigma \mathrm{d}\dot{V}$) for the individual drainage basins (Rignot et al., 2011a, b) indicated in Fig. 1 and the major Antarctic sectors (EAIS, WAIS and AIS) by integrating the estimated elevation change trends ($\mathrm{d}\dot{h}$) over these areas. The EAIS sector comprises basins A-A', A'-B, B-C, C-C', C'-D, D-D', D'-E, E-E', J"-K and K-A, while the WAIS sector comprises basins E'-F, G-H and J-J" (Fig. 1). The elevation change uncertainties ($\sigma_{\mathrm{d}\dot{h}}$) associated with the individual grid cells j lying within the integration area are propagated to estimate the uncertainty in volume change trend as

$$\sigma_{\Sigma \mathrm{d}\dot{V}} = \beta \sum (\sigma^2_{\mathrm{d}\dot{h}_j} \cdot A_j^2). \tag{13}$$

Here, A_j are the grid cell areas on the ellipsoid. The scaling factor β accounts for spatial error correlations. It is defined as the ratio of the error correlation area (A_{corr}) to the area of one grid cell ($A_{\mathrm{cell}} \approx 25\,\mathrm{km}^2$). The error correlation area is derived to be $A_{\mathrm{corr}} = 2\pi R^2$ based on the integration of a two-dimensional Gaussian function, where R denotes the spatial correlation length of the trend error.

For a realistic spatial pattern of the trend error, we use the difference in the trend between ICESat-2 and CryoSat-2 OCOG10 over their common time period. We calculate the spatial autocovariance of this trend difference for each drainage basin individually and determine R by applying a threshold of $1/\exp 1 \approx 0.37$ (e-folding length) to the empirical autocorrelation to account for an exponential correlation decay. For the major Antarctic sectors aggregated from several basins, R is derived from the area-weighted average of the associated, individual basin R values. The basin and sector values of R are listed in Table 3.

https://doi.org/10.5194/egusphere-2025-5745
Preprint. Discussion started: 15 December 2025

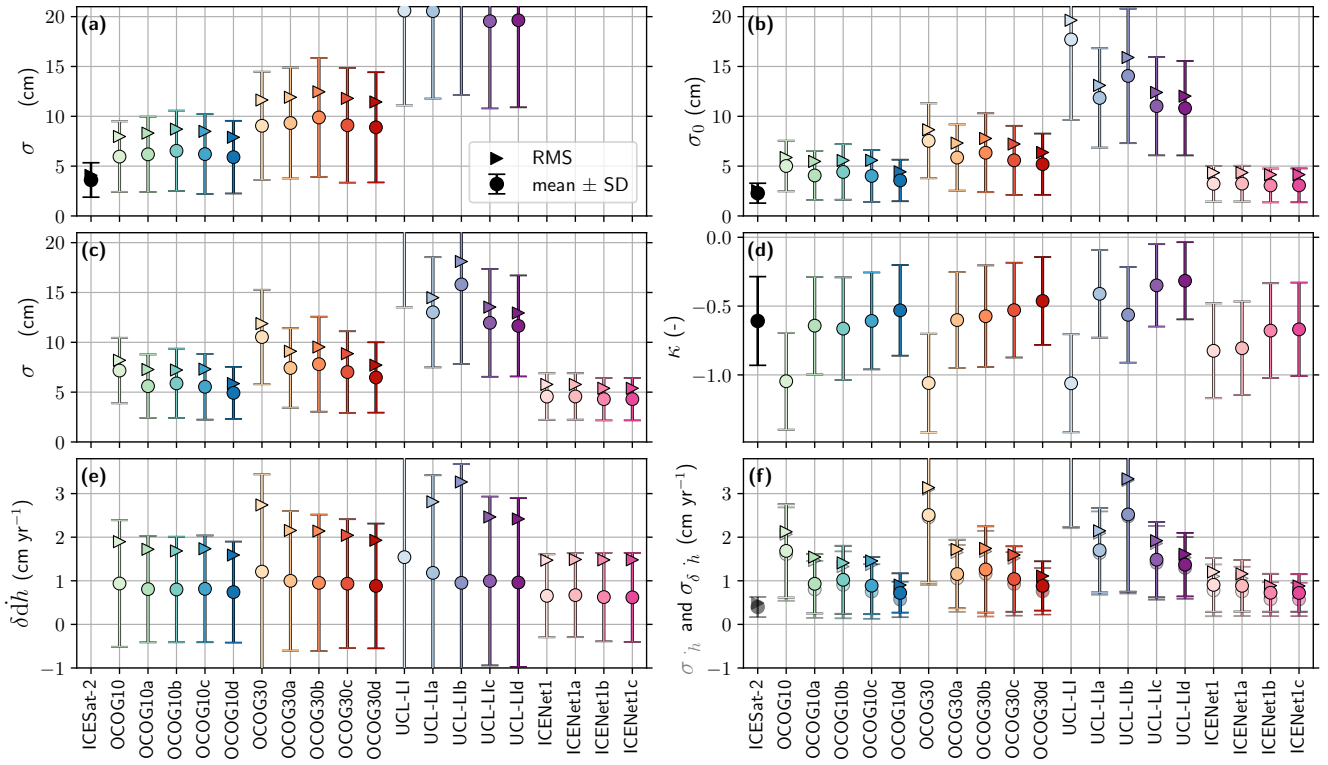

Figure 4. Statistics (mean, SD, RMS) of the metrics for the assessment of altimetry datasets (see also Table 2) estimated over all grid cells for the period from April 2019 to October 2024: (a) precision (σ_{AD}) and (c) accuracy (σ_{IC}), (b) noise level (σ_0) and (d) spectral index (κ) for power-law noise, (e) CryoSat-2 trend error ($\delta\dot{h}$) and (f) its associated uncertainty ($\sigma_{\delta\dot{h}}$). In addition, (f) shows the individual trend uncertainty ($\sigma_{\dot{h}}$) in transparent colours, which depends on σ_0 and κ. The SD is calculated as 1.253 times the mean absolute deviation to ensure robustness against outliers.

6 Results and discussion

6.1 Precision and accuracy

Figure 3a and b shows the precision (σ_{AD}) for ICESat-2 and CryoSat-2 OCOG10d, respectively. CryoSat-2 OCOG10d reveals larger σ_{AD} values than ICESat-2 with mean values of $5.9 \pm 3.6\,\mathrm{cm}$ vs. $3.6 \pm 1.7\,\mathrm{cm}$ over all grid cells of the LRM zone. For both datasets, but particularly for CryoSat-2, the spatial pattern of σ_{AD} seems related to the surface slope and roughness (Fig. 1). Comparing all 15 CryoSat-2 results reveals that the choice of the retracker has the greatest impact on the σ_{AD} value (Figs. 4a and S3). RMS values of σ_{AD} over all grid cells are in the range of 7.9 to 8.7 cm, 11.4 to 12.5 cm and 22.0 to 24.4 cm for OCOG10, OCOG30 and UCL-LI, respectively. Thus, while the different retrackers lead to differences in precision at the decimetre level, the different scattering corrections amount to differences at the millimetre or, at most, centimetre level. With

https://doi.org/10.5194/egusphere-2025-5745
Preprint. Discussion started: 15 December 2025

the retracker OCOG10 and the scattering correction d, using monthly differences of both BS and LEW (Table 1), the precision is best among our (conventional) radar altimetry results.

Figure 3c and d shows the accuracy (σ_{IC}) for CryoSat-2 OCOG10d and AWI-ICENet1c, respectively. Overall, the OCOG10d values are larger than AWI-ICENet1c with mean values of $4.9 \pm 2.6\,\mathrm{cm}$ vs. $4.3 \pm 2.1\,\mathrm{cm}$. The spatial pattern of σ_{IC} is similar to that of CryoSat-2 σ_{AD} (Fig. 3b), with higher values in areas of more complex topography. A comparison of all 19 CryoSat-2 results shows that again the choice of the retracker has the largest impact on the σ_{IC} value (Figs. 4c and S4). RMS values of σ_{IC} over all grid cells are lowest for AWI-ICENet1 (5.4 to $5.8\,\mathrm{cm}$), followed by OCOG10 (5.9 to $8.2\,\mathrm{cm}$) and OCOG30 (7.7 to $11.9\,\mathrm{cm}$), and are largest for UCL-LI (12.9 to $26.1\,\mathrm{cm}$). Within each of the three groups of conventional retrackers, the most accurate of the different scattering corrections is d. Thus, working with monthly differences improves the results in general. The correlations between dh and the waveform parameters, as shown in the Fig. 2, provided previous support for this already. Locally, this is most evident for the WAIS (Fig. S4). While the scattering correction is essential for improving the results of the conventional retrackers (Nilsson et al., 2022), it hardly has an influence on the AWI-ICENet1c solutions. The less sensitive the retracker is to changes in surface to volume scattering, the less necessary the scattering correction becomes (Helm et al., 2024).

6.2 ICESat-2 trend alongside GEMB

From April 2019 to October 2024, the ICESat-2 results reveal a volume increase of $97 \pm 4\,\mathrm{km^3\,yr^{-1}}$ for the entire LRM zone, with the EAIS and WAIS sectors contributing 93 ± 3 and $5 \pm 2\,\mathrm{km^3\,yr^{-1}}$, respectively. The ICESat-2 trend for the WAIS basins G-H and E'-F is strongly influenced by ice flow dynamics. For basin G-H, the GEMB trend pattern shows firn thickening throughout (Fig. 5d); therefore, the decreasing ICESat-2 trend (Fig. 5a) is most likely due to an underlying increase in ice flow from the glaciers of the Amundsen Sea sector. Apart from the linear trend, the temporal variations in volume change of basin G-H (Fig. 6j) match between ICESat-2 and GEMB. Until mid-2020, the increase in elevation coincides with extreme snowfall reported by Adusumilli et al. (2021) and Davison et al. (2023), which they associate with atmospheric rivers that occurred during the 2019 and 2020 austral winters. For basin E'-F, the ICESat-2 trend pattern clearly highlights the thickening of the stagnant Kamb Ice Stream (Nield et al., 2016), while the surrounding areas show a strong negative elevation trend. The GEMB trend is negative throughout basin E'-F.

In the following, we focus on basins where elevation changes are primarily driven by changes in firn and SMB processes and hardly influenced by ice flow dynamics. These basins include the entire EAIS sector and the WAIS basin J–J". We refer to these as "non-D" basins. Across the non-D basins, the spatial trend patterns of ICESat-2 and GEMB are similar (Figs. 5a and d), demonstrating widespread firn thickening. Only in some sub-areas of basins D-D', D'-E and E-E' the surface elevation decreases slightly. The entire area integrated volume trend of these basins is close to zero (Table 3). The most pronounced thickening, with ICESat-2 trends $\dot{\mathrm{d}}h > 5\,\mathrm{cm\,yr^{-1}}$, occurs in the northern part of basin J–J" and towards the ice sheet margins of basins K-A, C-C' and C'-D. The two basins that contribute the most to the overall non-D ICESat-2 trend in volume change (together accounting for more than half) are J"-K with $27 \pm 1\,\mathrm{km^3\,yr^{-1}}$ and C'-D with $25 \pm 2\,\mathrm{km^3\,yr^{-1}}$. The associated time

https://doi.org/10.5194/egusphere-2025-5745
Preprint. Discussion started: 15 December 2025

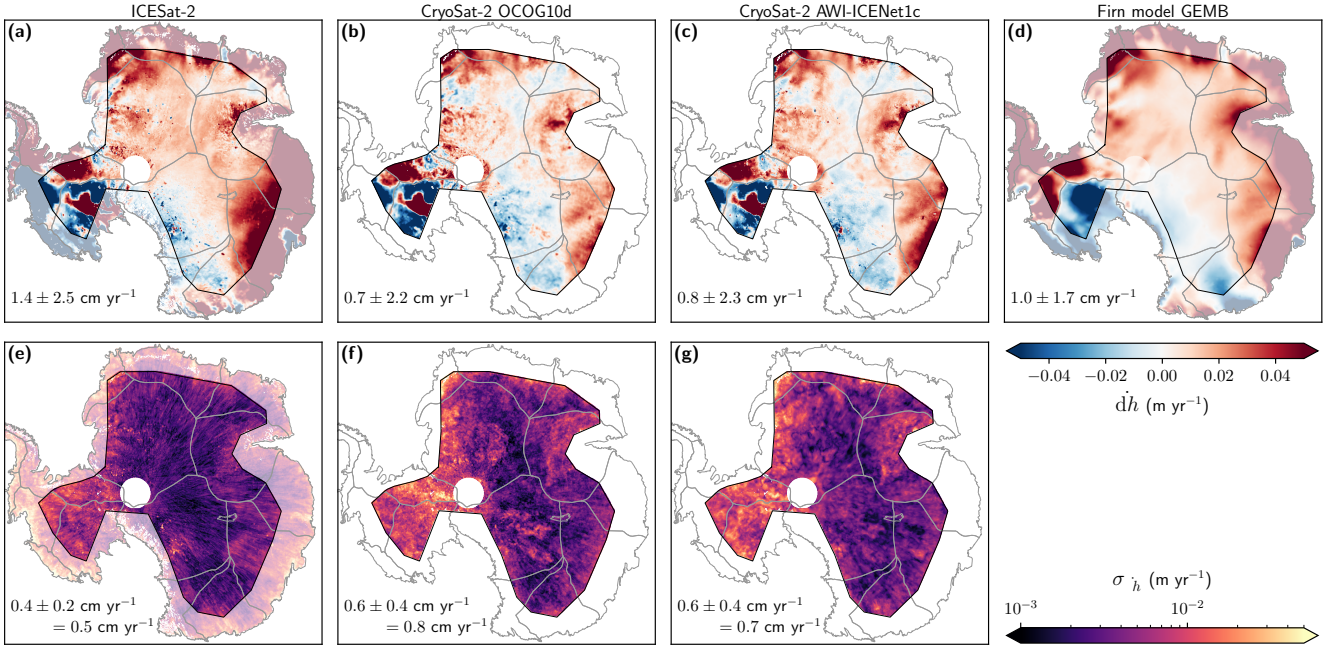

Figure 5. (a–d) Trends in surface elevation change ($\dot{dh}$) and (e–g) their uncertainty estimates ($\sigma_{\dot{dh}}$) calculated according to Eq. (12) for April 2019–October 2024. The estimates are shown for (a, e) ICESat-2, (b, f) CryoSat-2 OCOG10d, (c, g) CryoSat-2 AWI-ICENet1c and (d) the GEMB model. The mean ± SD, as well as the RMS for $\sigma_{\dot{dh}}$, are stated in the lower left corner for the entire LRM zone. Trend estimates for all altimetry datasets are shown by Figs. S5 and S6.

series of GEMB height changes exhibit a lower amplitude than ICESat-2 (Figs. 6l and e), which leads to less pronounced positive trends (Fig. 5d, Table 3).

The time series in volume change for the non-D basins show that extreme precipitation events, which are most likely causing the trend increases, occurred during different time periods. The time series for basins C-C' and C'-D show a striking increase in elevation between mid-2021 and the end of 2022 (Figs. 6d and e). This may be linked to the three-year La Niña event of 2021–2023, for which Wang et al. (2025) found that tropical-Antarctic teleconnections were enhanced and poleward atmospheric transport of heat and moisture was enabled. According to their study, these conditions led to increased snowfall, particularly in the area of basins C-C' and C'-D. The elevation increases in March 2022 coincide with the widely discussed heatwave accompanied by unprecedented snowfall events that affected large parts of East Antarctica, notably Queen Mary Land and Wilkes Land (Blanchard-Wrigglesworth et al., 2023; Clem et al., 2023; Wang et al., 2023; Wille et al., 2024b, a). The time series for basins J"-K and K-A show a prominent increase in elevation throughout the year 2023 (Figs. 6l and m). The time series for basins A-A' and A'-B show an increase in elevation from mid-2024 to end 2024 (Figs. 6a and b) coinciding with an exceptionally warm austral late winter in 2024 over eastern Dronning Maud Land and Enderby Land, as reported by Zhai et al. (2025).

https://doi.org/10.5194/egusphere-2025-5745
Preprint. Discussion started: 15 December 2025

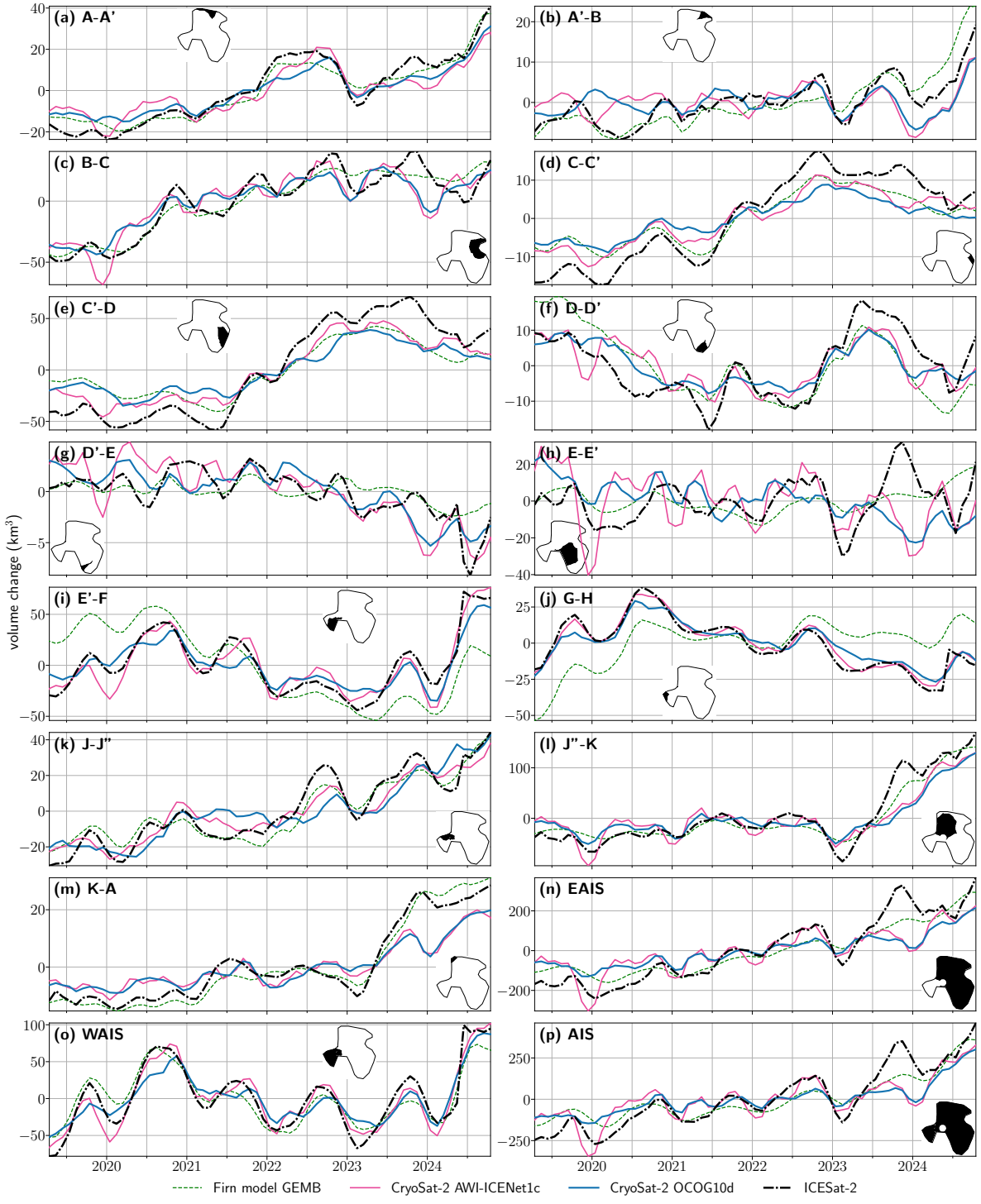

Figure 6. Volume change time series from different datasets (see legend) for the (a–m) individual drainage basins and (n–p) major sectors (as subregions of the LRM zone). The black area on the map in each panel shows the respective drainage basin or sector. Three-month moving averages are applied for visualisation purposes only.

https://doi.org/10.5194/egusphere-2025-5745
Preprint. Discussion started: 15 December 2025

Table 3. Results per AIS drainage basin or sector (LRM zone only) between April 2019 and October 2024: the observed area (A), spatial correlation length of the trend error (R) estimated as explained in Sect. 5.2.3, trend estimates in volume change ($\Sigma \mathrm{d}\dot{V}$) for the three main altimetry datasets (ICESat-2, CryoSat-2 OCOG10d and AWI-ICENet1c) and the GEMB firn model, and regression parameters offset and scale estimated to fit the ICESat-2 trend to the CryoSat-2 trend error (discussed in Sect. 6.5).

			ICESat-2	CryoSat-2 OCOG10d			CryoSat-2 AWI-ICENet1c			GEMB
Basin/ Sector	A (km^2)	R (km)	$\Sigma \mathrm{d}\dot{V}$ ($\mathrm{km}^3\,\mathrm{yr}^{-1}$)	$\Sigma \mathrm{d}\dot{V}$ ($\mathrm{km}^3\,\mathrm{yr}^{-1}$)	offset ($\mathrm{cm\,yr}^{-1}$)	scale (-)	$\Sigma \mathrm{d}\dot{V}$ ($\mathrm{km}^3\,\mathrm{yr}^{-1}$)	offset ($\mathrm{cm\,yr}^{-1}$)	scale (-)	$\Sigma \mathrm{d}\dot{V}$ ($\mathrm{km}^3\,\mathrm{yr}^{-1}$)
A-A'	339 500	200	9 ± 1	6 ± 2	-0.1	0.37	6 ± 2	0.3	0.25	8
A'-B	244 700	215	2 ± 1	0 ± 2	0.2	0.56	0 ± 2	0.5	0.44	4
B-C	955 400	100	14 ± 1	11 ± 1	-0.2	0.38	11 ± 1	0.0	0.18	15
C-C'	143 900	260	6 ± 1	2 ± 1	-0.2	0.65	4 ± 1	0.1	0.40	3
C'-D	623 100	190	25 ± 2	12 ± 2	-0.3	0.60	16 ± 2	0.4	0.24	12
D-D'	336 700	55	1 ± 0	-1 ± 0	0.6	0.19	-1 ± 0	0.6	0.08	-3
D'-E	153 800	65	-1 ± 0	-1 ± 0	0.6	0.65	-2 ± 0	0.7	0.54	0
E-E'	1 333 300	90	2 ± 1	-5 ± 1	0.5	0.37	-4 ± 1	0.4	0.37	1
J-J"	295 400	125	11 ± 2	10 ± 3	-0.4	0.22	9 ± 2	-0.4	0.29	9
J"-K	1 784 500	105	27 ± 1	15 ± 2	0.1	0.42	16 ± 2	0.0	0.38	21
K-A	94 500	80	7 ± 1	4 ± 1	-0.8	0.53	4 ± 1	-0.6	0.51	8
non-D[a]	6 304 800	120	104 ± 3	52 ± 6	0.2	0.37	59 ± 5	0.2	0.31	77
E'-F	461 400	60	1 ± 1	-1 ± 1	0.4	0.01	2 ± 1	-0.2	0.02	-17
G-H	138 800	110	-7 ± 1	-4 ± 1	-1.4	0.08	-6 ± 1	-0.4	0.06	7
EAIS	6 009 400	120	93 ± 3	43 ± 5	0.2	0.43	50 ± 5	0.2	0.33	68
WAIS	895 600	90	5 ± 2	4 ± 3	0.1	0.05	5 ± 3	0.0	0.05	-2
AIS	6 905 000	115	97 ± 4	47 ± 6	0.5	0.14	55 ± 6	0.4	0.12	67

[a] The non-D basins comprise all basins that are hardly influenced by ice flow dynamics; that is, EAIS with basin J–J", or in other words, AIS without basins E'-F and G-H.

https://doi.org/10.5194/egusphere-2025-5745
Preprint. Discussion started: 15 December 2025

Table 4. Trend estimates in volume change (given in $\mathrm{km^3\,yr^{-1}}$) over the period from April 2019 to October 2024 and the entire LRM zone for all 19 different CryoSat-2 results.

Correction \ Retracker	OCOG 10	OCOG 30	UCL-LI	AWI-ICENet1
–	33 ± 16	14 ± 24	-10 ± 56	52 ± 9
a	42 ± 11	29 ± 13	16 ± 16	51 ± 8
b	42 ± 10	32 ± 13	31 ± 26	55 ± 6
c	42 ± 11	33 ± 12	29 ± 14	55 ± 6
d	47 ± 6	37 ± 8	31 ± 12	

6.3 CryoSat-2 trends and errors

The trend estimates in volume change from CryoSat-2 show a large spread depending on the chosen retracking algorithm and scattering correction (Table 4). For the entire LRM zone and the overlapping time period with ICESat-2 (April 2019–October 2024), the estimates range from -10 ± 56 to $55 \pm 6\,\mathrm{km^3\,yr^{-1}}$. The latter is derived from AWI-ICENet1c, identified as the most accurate of all the CryoSat-2 results (Sect. 6.1, Fig. 4c). Yet, the AWI-ICENet1c trend is $42\,\mathrm{km^3\,yr^{-1}}$ smaller than the ICESat-2 trend. The most accurate solution of the conventional retrackers, OCOG10d, provides a trend in volume change of $47 \pm 6\,\mathrm{km^3\,yr^{-1}}$. Trend maps of both, OCOG10d and AWI-ICENet1c, are given in Figs. 5b and c, respectively.

To assess the error in CryoSat-2 trends, we calculate the trend differences ICESat-2−CryoSat-2 ($\delta \mathrm{d}\dot{h}$) as described in Sect. 5.2.2. Figure 4e shows the statistics for $\delta \mathrm{d}\dot{h}$ estimated over all grid cells for each dataset. As with σ_{IC} (Fig. 4c), RMS values of $\delta \mathrm{d}\dot{h}$ are lowest for the four solutions from AWI-ICENet1 ($1.5\,\mathrm{cm\,yr^{-1}}$), followed by the five solutions from OCOG10 (1.6 to $1.9\,\mathrm{cm\,yr^{-1}}$) and OCOG30 ($1.9$ to $2.7\,\mathrm{cm\,yr^{-1}}$), and are largest for the five solutions from UCL-LI (2.4 to $5.4\,\mathrm{cm\,yr^{-1}}$).

In the following, we present the spatial distribution of $\delta \mathrm{d}\dot{h}$. First, the trend differences between ICESat-2 and CryoSat-2 OCOG30a (Fig. 7a) are shown, because OCOG30a represents a standard approach in radar altimetry analysis, with retracked elevations from the ESA L2I product corrected for the correlation with the BS variations. Fig. 7b then shows $\delta \mathrm{d}\dot{h}$ using CryoSat-2 OCOG10a. Comparison of Fig. 7a with b demonstrates the improvement by using a lower threshold since $\delta \mathrm{d}\dot{h}$ for OCOG30 is overall larger than for OCOG10 (in an absolute sense) throughout the study area. The mean trend errors are 1.0 ± 1.6 and $0.8 \pm 1.2\,\mathrm{cm\,yr^{-1}}$ for OCOG30a and OCOG10a, respectively.

The impact of using an enhanced scattering correction on the trend estimate is demonstrated by comparing Fig. 7b with c. The latter shows $\delta \mathrm{d}\dot{h}$ using the OCOG10d results, which yield the lowest trend errors among the conventional retracking algorithms (Fig. 4e). The mean trend error reduces slightly to $0.7 \pm 1.2\,\mathrm{cm\,yr^{-1}}$ when correction d is used instead of correction a. Overall, correction d reveals the lowest trend error within each group of conventional retrackers (Fig. 4e), which aligns with the time-series-based precision and accuracy results. The improvement from OCOG10a to OCOG10d is rather localised to certain regions. It is most pronounced at the thickening of the Kamb Ice Stream (where $\delta \mathrm{d}\dot{h}$ is less negative) and the northern

https://doi.org/10.5194/egusphere-2025-5745
Preprint. Discussion started: 15 December 2025

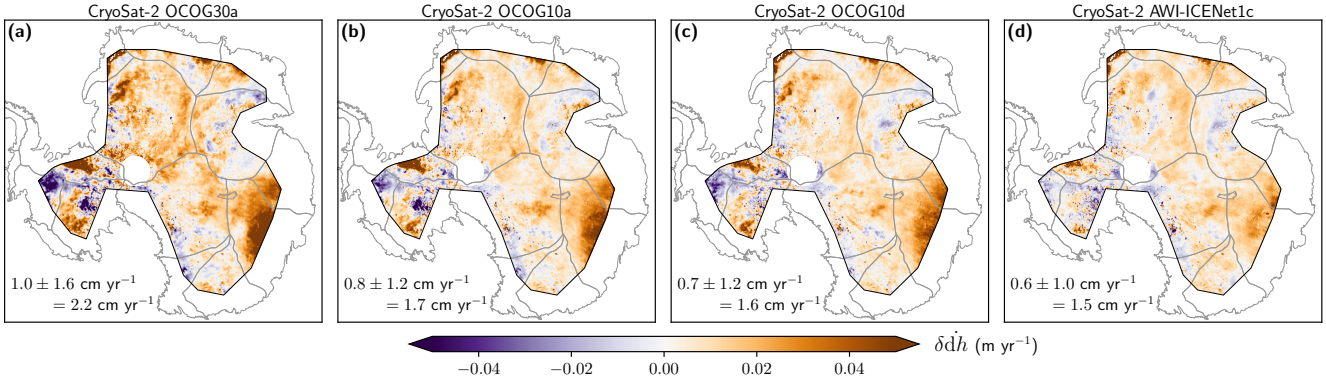

Figure 7. Trend errors ($\delta\dot{dh}$) for (a) OCOG30a, (b) OCOG10a, (c) OCOG10d and (d) AWI-ICENet1c calculated from the trend differences ICESat-2−CryoSat-2. The mean ± SD and RMS for the entire LRM zone are stated in the lower left corner. Trend errors for all CryoSat-2 datasets are shown by Fig. S7.

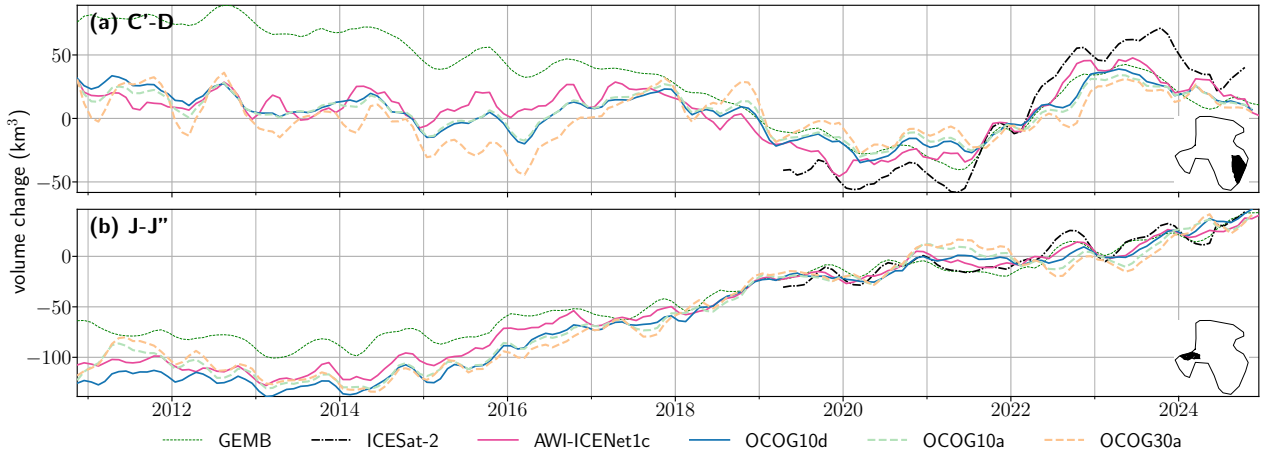

Figure 8. Volume change time series from various CryoSat-2 solutions (see legend) for two selected drainage basin subregions of the LRM zone, (a) C'-D and (b) J-J", and the period from November 2010 to December 2024. The black area on the map in each panel shows the respective drainage basin. Three-month moving averages are applied for visualisation purposes only. Time series for all drainage basin subregions from November 2010 are shown by Figs. S8 and S9.

part of basin J–J" (where $\delta\dot{dh}$ is less positive). Figure 8b shows the temporal development of the volume change of basin J–J" for the entire CryoSat-2 period.

Comparison of Fig. 7c and d illustrates the impact of using the novel AWI-ICENet1 retracker rather than a conventional one. With AWI-ICENet1c, the mean trend error further decreases to $0.6 \pm 1.0\,\mathrm{cm\,yr^{-1}}$. Locally, the improvement of AWI-ICENet1 is most striking over the WAIS and for basins C-C' and C'-D. The C'-D basin time series in volume change (Fig. 8a) show that, despite the lower amplitude and slight temporal shifts, AWI-ICENet1 most closely aligns with the ICESat-2 time series.

https://doi.org/10.5194/egusphere-2025-5745
Preprint. Discussion started: 15 December 2025

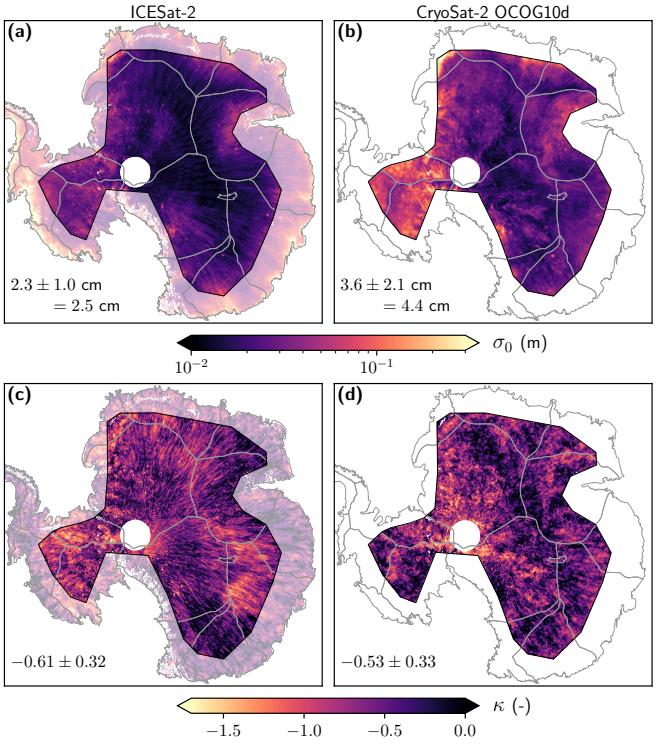

Figure 9. (a, b) Noise level (σ_0) and (c, d) spectral index (κ) for power-law noise of (a, c) ICESat-2 and (b, d) CryoSat-2 OCOG10d. The mean ± SD, and RMS for σ_0, are stated in the lower left corner for the entire LRM zone.

6.4 Trend uncertainties

Maps of the standard uncertainty of the trend ($\sigma_{\dot{dh}}$) for the three best and most discussed altimetry datasets are shown in Fig. 5. Overall, their mean trend uncertainties are $0.4 \pm 0.2\,\mathrm{cm\,yr^{-1}}$ for ICESat-2 (Fig. 5e) and $0.6 \pm 0.4\,\mathrm{cm\,yr^{-1}}$ for CryoSat-2 OCOG10d (Fig. 5f) as well as AWI-ICENet1c (Fig. 5g). As with σ_{AD} and σ_{IC} (Fig. 3), the spatial pattern of $\sigma_{\dot{dh}}$ also appears to be related to the surface slope and roughness (Fig. 1). However, to better understand the pattern of $\sigma_{\dot{dh}}$, we need to consider the two noise parameters: the noise level (σ_0) and the spectral index (κ) for power-law noise. These parameters describe the altimetry noise, which we defined as anything that could not be explained by GEMB firn height changes or a linear trend (Sect. 5.2.1), and they control the estimation of $\sigma_{\dot{dh}}$. Figure 9 illustrates the spatial pattern of these parameters and their interplay and impact on $\sigma_{\dot{dh}}$. It shows that the link between $\sigma_{\dot{dh}}$ and the slope originates from σ_0. The noise level (σ_0) of all altimetry datasets (Figs. 4b and S11) follows the order already discussed for σ_{AD} and σ_{IC}. ICESat-2 has the lowest RMS values ($2.5\,\mathrm{cm}$). These are followed by the CryoSat-2 AWI-ICENet1 (4.1 to $4.4\,\mathrm{cm}$), OCOG10 (4.4 to $5.9\,\mathrm{cm}$) and OCOG30 (6.4 to $8.7\,\mathrm{cm}$) solutions. The UCL-LI solutions have the largest RMS values (12.0 to $19.6\,\mathrm{cm}$).

On average, the altimetry time series exhibit a temporal correlation behaviour between white and flicker noise, since mean values of κ are -0.61 ± 0.32 and -0.53 ± 0.33 for ICESat-2 and CryoSat-2 OCOG10d, respectively. Assuming that non-linear

https://doi.org/10.5194/egusphere-2025-5745
Preprint. Discussion started: 15 December 2025

signals — apart from variations due to SMB and firn processes, which should be captured by GEMB — play a subordinate role across the LRM zone, the occurrence of correlated noise in the ICESat-2 time series might indicate that the GEMB model is missing or imperfectly (e.g. with different amplitude) modelling SMB and firn variations. This would mean that the ICESat-2 noise remains with real, temporally correlated signal. Temporal correlation is intensified mainly across basins J–J" and C'-D (Fig. 9c), where ICESat-2 yields most negative values ($\kappa < -1.0$). See also Fig. S1 for example series in the time and frequency domains of a grid cell in the C'-D basin. It would further imply that the ICESat-2 trend uncertainty could be somewhat overestimated at grid cell level.

The spatial pattern of κ for CryoSat-2 OCOG10d is different to that for ICESat-2. CryoSat-2 OCOG10d yields strong correlated noise ($\kappa < -1.0$) mainly around the pole and in certain regions of basins J"-K and E-E' (Fig. 9d). See also Fig. S2 for example series in the time and frequency domains of a grid cell in the J"-K basin. It can be assumed that the remaining temporal correlation in the CryoSat-2 noise is considerably influenced by correlated errors related to time-variable radar signal penetration, alongside real SMB and firn signals (Kappelsberger et al., 2024). Moreover, applying a scattering correction has a strong influence on the value of κ (Fig. 4d), as it makes the altimetry time series "whiter", i.e. κ closer to 0. Comparing the estimates of κ between the different conventional retrackers, OCOG30 and UCL-LI exhibit less negative values of κ than OCOG10 (Figs. 4d and S10), likely because the degree of temporal correlation is dampened by stronger underlying white noise.

We compared the trend uncertainties derived from using the power-law noise model with those derived from using a white noise model ($\kappa = 0$) only. Depending on the altimetry dataset investigated, the white noise model would generate uncertainties too small by a median factor ranging from 1.4 to 3.0. Specifically for ICESat-2 and CryoSat-2 OCOG10d, assuming temporal uncorrelated time series (white noise) would lead to an underestimation of the trend uncertainty by factors of 1.9 and 1.8, respectively.

6.5 Potential causes of trend errors

We noticed a dependency on the slope of the ice sheet surface (Fig. 1) for several metrics that assessed the altimetry results, namely the precision (σ_{AD}, Fig. 3a and b), accuracy (σ_{IC}, Fig. 3c and d), noise level (σ_0, Fig. 9a and b) and trend uncertainty ($\sigma_{\dot{dh}}$, Fig. 5e–g). Exemplary, Fig. 10a illustrates the spatial relationship between the surface slope and σ_0 for CryoSat-2 OCOG10d. For the other metrics, the spatial relationship with the surface slope is further confirmed and illustrated in Fig. S12. Correlation coefficients between the surface slope and these metrics range from 0.43 for ICESat-2 $\sigma_{\dot{dh}}$ to 0.71 for CryoSat-2 OCOG10d σ_0. We also test for a spatial relationship between the CryoSat-2 trend error ($\delta\mathrm{d}\dot{h}$, Fig. 7) and the surface slope. The mean $\delta\mathrm{d}\dot{h}$ for different slope bins does not reveal a relationship. However, the SD of $\delta\mathrm{d}\dot{h}$ for different slope bins indicates an influence of topography, in that the spread increases from smaller to larger slopes (Fig. 10b).

Over our rather flat study area, the laser-radar trend differences suggest that the radar results are affected by temporal changes in the radar waveform shape, which in turn is affected by changes in the ice sheet surface and subsurface properties. For this reason, we investigate several atmospheric and snow parameters from the monthly averages of the ERA5 global reanalysis (Hersbach et al., 2020): $10\,\mathrm{m}$ wind speed and its eastward and northward components, $10\,\mathrm{m}$ wind gust, surface temperature,

https://doi.org/10.5194/egusphere-2025-5745
Preprint. Discussion started: 15 December 2025

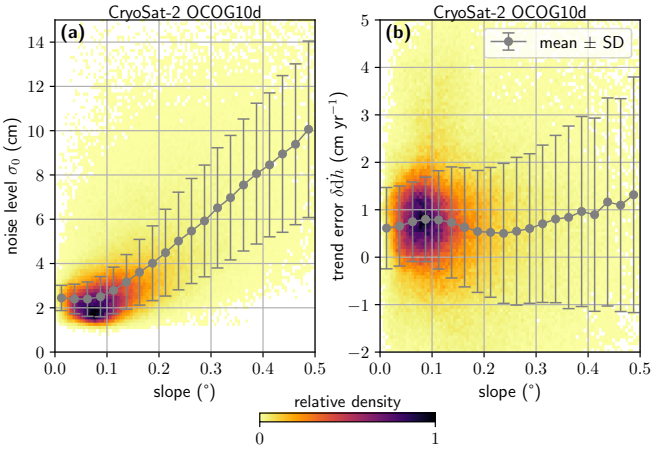

Figure 10. The AIS surface slope plotted against (a) the noise level (σ_0) and (b) the trend error ($\delta\dot{d}\dot{h}$) of CryoSat-2 OCOG10d. The number of grid cells belonging to one colour-coded pixel is shown from a few (yellow-white) to many (deep purple) cells. Mean and SD values are calculated at $0.025°$ slope bins, thus 20 intervals between 0.0 and $0.5°$.

and temperature of the snow layer. We calculate the trends in temporal changes of these ERA5 parameters over the same period and area, and compare their spatial patterns with the $\delta\dot{d}\dot{h}$ pattern. However, we do not find any relationships (Figs. S13 and S14). We perform the same investigation with the GEMB firn height changes and their two components, changes due to FAC and SMB. We also examine additional outputs from the firn model IMAU-FDM v1.2A (Veldhuijsen et al., 2023), including $10\,\mathrm{m}$ firn temperature and surface snow density. The trend field of firn temperature does not show a clear relationship with $\delta\dot{d}\dot{h}$ (Fig. S15a–c, correlation coefficient ≈ 0.2). Correlation with $\delta\dot{d}\dot{h}$ is somewhat larger for the trends in surface snow density, FAC and SMB changes, and total firn height changes (Figs. S15d–f and S16, correlation coefficients ≈ 0.3). The latter trend estimate has already been presented in Fig. 5d, and its spatial pattern is shared by both of its components (Figs. S16a and d). Enhanced snowfall, the main component of SMB in Antarctica, increases the trend in both modelled SMB and FAC height changes over most of our study area, the latter being due to less dense firn.

Next, we investigate $\delta\dot{d}\dot{h}$ in relation to the ICESat-2 trend (Fig. 5a) representing the "true" signal. Indeed, we find a closer relationship between the spatial pattern of $\delta\dot{d}\dot{h}$ and the ICESat-2 trend than with the model outputs. The correlation coefficient is 0.40 for the whole LRM area and rises to 0.64 for the areas predominantly influenced by firn and SMB processes, the non-D basins (based on OCOG10d $\delta\dot{d}\dot{h}$). Figure 11a and b illustrates this relationship. We model this relationship as a regression line using

$$\delta\dot{d}\dot{h}_i = b_0 + b_1\,\dot{d}\dot{h}_i + \epsilon_i. \tag{14}$$

Here, $\dot{d}\dot{h}$ refers to the ICESat-2 trend, b_0 and b_1 are the adjusted parameters offset and scale factor, respectively, and ϵ are the residuals. We conduct a regression for each basin and sector as well as for $\delta\dot{d}\dot{h}$ based on CryoSat-2 OCOG10d and AWI-ICENet1c (Figs. S17 and S18). The adjusted parameters, offset (b_0) and scale factor (b_1), are listed in Table 3. The scale factors derived for the two WAIS basins that are strongly influenced by ice flow dynamics (E'-F and G-H) are almost zero for both

https://doi.org/10.5194/egusphere-2025-5745
Preprint. Discussion started: 15 December 2025

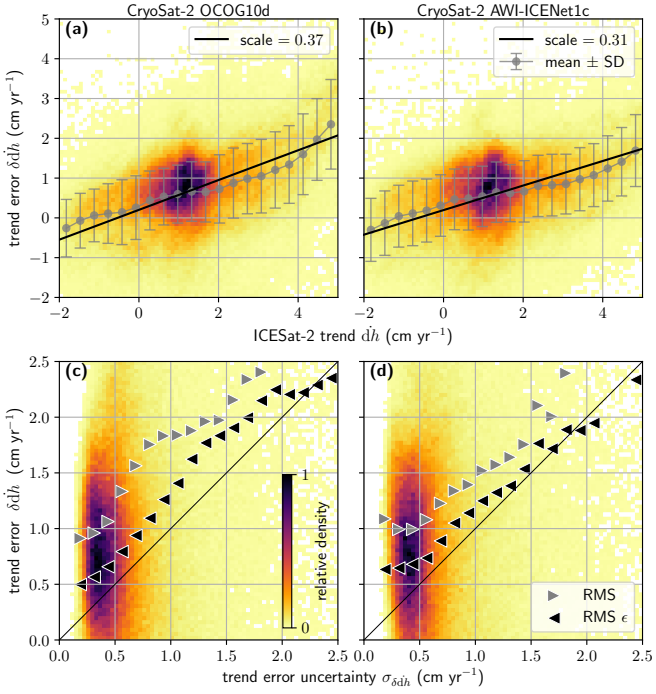

Figure 11. (a, b) The ICESat-2 trend plotted against the CryoSat-2 trend error ($\delta\dot{dh}$), using (a) OCOG10d and (b) AWI-ICENet1c for the non-D basins. Mean and SD values are calculated at $0.35\,\mathrm{cm\,yr^{-1}}$ trend bins, thus 20 intervals between -2 and $5\,\mathrm{cm\,yr^{-1}}$. The black line shows the adjusted regression line (Eq. 14). (c, d) The standard uncertainty of the trend error ($\sigma_{\delta\dot{dh}}$) plotted against the absolute trend error ($|\delta\dot{dh}|$), using (c) OCOG10d and (d) AWI-ICENet1c for the non-D basins. RMS values are calculated at $0.125\,\mathrm{cm\,yr^{-1}}$ uncertainty bins, thus 20 intervals between 0.0 and $2.5\,\mathrm{cm\,yr^{-1}}$. The grey, right-pointing triangles and the black, left-pointing triangles show the RMS values for $\delta\dot{dh}$ and the residuals (ϵ in Eq. 14), respectively. The number of grid cells belonging to one colour-coded pixel is shown from a few (yellow-white) to many (deep purple) cells.

CryoSat-2 datasets. For the non-D basins (except for basin D-D' with AWI-ICENet1c), throughout clear positive scale factors ranging from 0.18 to 0.65 are determined.

The regression of all values within the non-D area estimates an offset of $0.2\,\mathrm{cm\,yr^{-1}}$ and scale factors of 0.37 and 0.31 for OCOG10d and AWI-ICENet1c, respectively (Table 3). Figure 11a and b displays their adjusted regression lines. A trend offset in elevation change of $0.2\,\mathrm{cm\,yr^{-1}}$ between ICESat-2 and CryoSat-2 is small. The throughout positive scale factors suggest that the elevation changes across the flat Antarctica interior, which predominantly show increases coinciding with several snowfall events over the period from April 2019 to October 2024, appear systematically smaller for CryoSat-2 than for ICESat-2. As loose, fresh snow introduces stronger radar signal penetration due to its lower density (Sørensen et al., 2015), CryoSat-2 might observe a lower rate of thickening than ICESat-2. The radar altimetry methods of retracking and scattering correction are designed to correct errors related to signal penetration removing the correlation between changes in the retracking point and changes in shape of the waveform. The most advanced methods do improve the CryoSat-2 results, but they may still be

https://doi.org/10.5194/egusphere-2025-5745
Preprint. Discussion started: 15 December 2025

imperfect. Specifically, they may not only reduce artefacts, but also remove real signal, since both originate from changes in the upper firn layer. In addition, slight trend offsets could be introduced in cases where the power and range are not perfectly calibrated. As the instrument ages, the transmit power usually reduces and the impulse response widens. The latter impacts the shape of the waveform. If a trend in LEW and/or BS exists, it will directly affect $\mathrm{d}\dot{h}$ when applying the corrections. Neither can be compensated by AWI-ICENet1.

The above hypothesis suggests that temporal variations in snow properties, particularly the addition of fresh snow, lead to stronger radar signal penetration inducing systematic errors. This assumes that newly fallen snow will remain "fresh" or loose for a while. Therefore, this hypothesis may be limited if katabatic winds quickly redistribute the new snow, as then the snow will also compact more quickly. To further explore hypotheses regarding the ICESat-2–CryoSat-2 trend differences, one might also question the ICESat-2 results. Differences between the basin time series of ICESat-2 and CryoSat-2 seem to be largest for the year 2023, over which ICESat-2 suggests a striking increase in EAIS surface elevation (Fig. 6). If the ICESat-2 laser measurements taken during 2023 were somehow biased for unknown reasons, this would also affect the 2019-2024 trend. However, further research and, ideally, additional data are needed to confirm one of our hypotheses or to find and confirm new ones. Further studies could e.g. incorporate measurements from other sensors, such as those from the SARAL/AltiKa mission, which uses a Ka-band altimeter (Verron et al., 2015). Furthermore, future studies involving coincident laser-radar measurements collected over a longer period could facilitate observation of a wider range of ice sheet processes. This might help to identify the causes of trend differences more comprehensively.

6.6 Evaluation of the trend uncertainties

The trend errors ($\delta\mathrm{d}\dot{h}$) can further be used to evaluate the standard uncertainties ($\sigma_{\delta\mathrm{d}\dot{h}}$), obtained from propagating the trend uncertainties ($\sigma_{\mathrm{d}\dot{h}}$) of ICESat-2 and CryoSat-2 (Sect. 5.2.2). First, we compare the RMS of $\delta\mathrm{d}\dot{h}$ with the RMS of $\sigma_{\delta\mathrm{d}\dot{h}}$ calculated over the entire area for all datasets (Fig. 4e vs. f). With the exception of the values from UCL-LIb and the non-scattering-corrected time series (OCOG10, OCOG30, UCL-LI), $\delta\mathrm{d}\dot{h}$ is larger than $\sigma_{\delta\mathrm{d}\dot{h}}$, suggesting that the standard uncertainties underestimate the true errors. For instance, RMS values of $\delta\mathrm{d}\dot{h}$ and $\sigma_{\delta\mathrm{d}\dot{h}}$ are 1.6 and $0.9\,\mathrm{cm\,yr^{-1}}$ for OCOG10d and 1.5 and $0.9\,\mathrm{cm\,yr^{-1}}$ for AWI-ICENet1c. This also affects the uncertainty of the area-integrated CryoSat-2 trend estimates, which do not reflect the trend difference with ICESat-2 (Table 3). Additionally, the uncertainties for area-integrated values are affected by rather rough assumptions and approximations about spatial error correlations.

Second, we have a closer look on the relationship between $\delta\mathrm{d}\dot{h}$ and $\sigma_{\delta\mathrm{d}\dot{h}}$ illustrated in Fig. 11c and d. The grey, right-pointing triangles depict the RMS values of $\delta\mathrm{d}\dot{h}$ calculated for different $\sigma_{\delta\mathrm{d}\dot{h}}$ bins. If the triangles were to lie on the black diagonal line, this would suggest reasonable uncertainty estimates and a perfect linear relationship with the SD of the true trend errors. However, the RMS values of $\delta\mathrm{d}\dot{h}$ are above the assessed uncertainties (through the various bins), supporting the suggestion in the previous paragraph that the uncertainties are underestimated. The black, left-pointing triangles depict the RMS values of the residuals (ϵ) of the regression (Eq. 14) for the different $\sigma_{\delta\mathrm{d}\dot{h}}$ bins. This reduces the previous discrepancy between uncertainty and error (overall RMS values of ϵ are $\approx 1.0\,\mathrm{cm\,yr^{-1}}$) and results in a more linear relationship. Thus, without modelling the systematics, our standard trend uncertainties are too small, despite our rather conservative assessment of

https://doi.org/10.5194/egusphere-2025-5745
Preprint. Discussion started: 15 December 2025

uncertainties that considers temporal correlation. Apart from the systematic differences, which can be modelled using an offset and a scale factor, the trend errors are within the assessed standard uncertainty estimate.

6.7 Comparison to other studies

In this study, we infer overall less positive trends (i.e. a smaller thickening) with CryoSat-2 than with ICESat-2 for all different retracking and scattering correction approaches (Fig. 4e). Using the most accurate CryoSat-2 result, the mean trend error (i.e. trend difference ICESat-2−CryoSat-2) is $0.6 \pm 1.0\,\mathrm{cm\,yr^{-1}}$ over 2019–2024 for the Antarctic LRM zone. In the Amundsen Sea sector of the WAIS, Yue et al. (2023) indicated a more negative trend (i.e. a stronger thinning) using CryoSat-2 than ICESat-2, with an average trend difference of $6.7\,\mathrm{cm\,yr^{-1}}$ for the period 2019–2021. By contrast, Ravinder et al. (2024) found that CryoSat-2 trends were less negative (i.e. smaller thinning) than ICESat-2 trends over the Greenland Ice Sheet. They estimated an average trend difference of $-3.3 \pm 6.0\,\mathrm{cm\,yr^{-1}}$ across Greenland's ablation zone for the period 2018–2022. However, it is difficult to compare these results with ours, as errors related to topography, sampling issues and interpolation compound errors related to radar signal penetration in areas of complex topography, such as Greenland's coastal ablation zone or the Amundsen Sea sector in Antarctica.

For Greenland's interior, Ravinder et al. (2024) estimated an average trend difference close to zero ($-0.2 \pm 1.5\,\mathrm{cm\,yr^{-1}}$). Even though the ice sheet topography is less complex there, this trend difference may not be comparable to our results for Antarctica's interior, as the processes leading to elevation changes in recent years have generally differed in the two regions. Excess accumulation events led to thickening of the AIS interior over 2019–2024 (Sect. 6.2). In contrast, the interior of the Greenland Ice Sheet (with an exception of the north-east) thinned over 2018–2022, primarily due to summer melting events (Ravinder et al., 2024), which can lead to sudden changes in the scattering horizons (Nilsson et al., 2015). Consequently, CryoSat-2 measurements are subject to different time-variable firn properties and elevation biases. Prior to the ICESat-2 mission, Sørensen et al. (2015) derived elevation trends from laser (ICESat) and radar (Envisat) altimetry for Greenland's interior over 2003–2009. Based on ICESat, they observed a small thickening in the interior and also found predominantly positive ICESat−Envisat trend differences. Similar to our investigations, they tested for relationships between the laser-radar trend differences and various outputs from global reanalysis data and regional firn modelling. At a local scale, trends in FAC and accumulation could explain some of the differences.

From April 2019 to October 2024, our CryoSat-2 volume change trends using the AWI-ICENet1 retracking results range from 51 ± 8 to $55 \pm 6\,\mathrm{km^3\,yr^{-1}}$ (Table 4), in contrast to the ICESat-2 trend of $97 \pm 4\,\mathrm{km^3\,yr^{-1}}$. For the same area but a shorter time period (January 2019–December 2021), Helm et al. (2024) stated that CryoSat-2 AWI-ICENet1 trends in volume change were between 84 ± 13 and $93 \pm 14\,\mathrm{km^3\,yr^{-1}}$, which corresponded to the ICESat-2 estimate of $96 \pm 6\,\mathrm{km^3\,yr^{-1}}$. In contrast to the positive ICESat-2 trend over 2019–2024, which was dominated by drastic thickening across the non-D basins (i.e. EAIS and J–J"), the overall positive ICESat-2 trend by 2021 was less influenced by the non-D basins (Fig. 6n and k) and more influenced by the two WAIS basins E'-F and G-H (Fig. 6i and j). The fact that the 2019–2021 area-integrated values from Helm et al. (2024) align (even considering smaller uncertainties), but the 2010–2024 values do not, is not due to smaller trend differences at grid cell level over this shorter period. Rather, it is due to more negative trend differences cancelling out the positive differences

https://doi.org/10.5194/egusphere-2025-5745
Preprint. Discussion started: 15 December 2025

in volume integration. For this reason, RMS values of the entire study area were used in Sect. 6.3 to indicate the CryoSat-2 dataset with the lowest trend error.

6.8 Implications for uncertainties in Antarctic volume and mass trends

CryoSat-2 observes the thickening in the AIS LRM zone at a lower rate of $0.6\,\mathrm{cm\,yr^{-1}}$ or $42\,\mathrm{km^3\,yr^{-1}}$ than ICESat-2, which is $43\,\%$ of the actual signal observed with ICESat-2 over 2019–2024. For the entire grounded AIS area of $12\,352\,700\,\mathrm{km^2}$ (including the islands; Rignot et al., 2019), an average trend difference of $0.6\,\mathrm{cm\,yr^{-1}}$ would translate into a trend error of $74\,\mathrm{km^3\,yr^{-1}}$ in radar altimetry results. This estimate exceeds the long-term AIS altimetry trend estimates and their uncertainties, as derived by Zhang et al. (2020) over 2002–2019 ($-69\pm8\,\mathrm{km^3\,yr^{-1}}$) and by Nilsson et al. (2022) over 1992–2020 ($-68\pm11\,\mathrm{km^3\,yr^{-1}}$). Nilsson et al. (2022) also incorporated systematic error estimates based on comparisons with an elevation change trend derived from ICESat and ICESat-2. Next, we aim to provide some rough estimates that demonstrate the further implications of the radar altimetry errors that we identified. Using an Antarctic average surface snow density of $376\,\mathrm{kg\,m^{-3}}$ (Veldhuijsen et al., 2023) for the volume-to-mass conversion, would lead to a trend error of $28\,\mathrm{Gt\,yr^{-1}}$. Using ice density ($917\,\mathrm{kg\,m^{-3}}$) would result in an error of $68\,\mathrm{Gt\,yr^{-1}}$. The latter estimate may be rather conservative, as our findings suggest that laser-radar trend differences are linked to greater radar signal penetration during snowfall events.

Previous mass balance estimates from altimetry were assigned uncertainties well below our error quantification. Shepherd et al. (2019) estimated mass trends of $16\pm6\,\mathrm{Gt\,yr^{-1}}$ and $-82\pm12\,\mathrm{Gt\,yr^{-1}}$ for the EAIS and WAIS, respectively, over 1992–2017 using multi-mission radar altimetry. Schröder et al. (2019) estimated mass trends of $5\pm5\,\mathrm{Gt\,yr^{-1}}$, $-92\pm10\,\mathrm{Gt\,yr^{-1}}$ and $-85\pm16\,\mathrm{Gt\,yr^{-1}}$ for the EAIS, WAIS, and AIS, respectively, over 1992–2017 using multi-mission radar altimetry and ICESat data. The Ice Sheet Mass Balance Inter-comparison Exercise (IMBIE) assesses the mass balance of the ice sheets for the three techniques (altimetry, gravimetry and input-output) both individually and in combination. The trend estimates and their uncertainties provided by IMBIE are of exceptional significance as they serve as a key source of information e.g. for the Assessment Report of the Intergovernmental Panel on Climate Change. The AIS mass trend estimated from the aggregated altimetry results in IMBIE was about $-86\pm7\,\mathrm{Gt\,yr^{-1}}$ over 2002–2019 (approximately as read from Fig. 3a in Otosaka et al., 2023b), with an uncertainty estimate roughly four times smaller than that of gravimetry.

In the light of our minimum AIS trend error of $28\,\mathrm{Gt\,yr^{-1}}$, the altimetry uncertainties of $\pm7\,\mathrm{Gt\,yr^{-1}}$ (Schröder et al., 2019) and $\pm16\,\mathrm{Gt\,yr^{-1}}$ (Otosaka et al., 2023b) appear unrealistically small and may not account for systematic errors. We acknowledge that our trend error estimate depends on the time period of this study and the (extent of) SMB and firn processes occurring over that period. Therefore, it could differ (being both smaller or larger) for other time periods. Nevertheless, we assume that our error estimate is rather optimistic for two reasons. First, if the CryoSat-2 bias we estimated for the LRM zone extends to the margins of the ice sheet and remains proportional to the actual trend signal, then the bias would increase at the margins. However, our error estimate only assumes a constant bias. Second, our trend error primarily reflects radar altimetry errors related to signal penetration. It would further increase when considering additional error sources. These sources include errors related to topography; which are more relevant at the ice sheet margins (e.g. due to undersampling of low-lying,

https://doi.org/10.5194/egusphere-2025-5745
Preprint. Discussion started: 15 December 2025

accelerating glaciers by radar altimetry systems); errors in the volume-to-mass conversion and errors due to intermission calibration; which are relevant for multi-mission altimetry estimates.

To independently validate our altimetry-derived estimates, we compare them with mass change estimates from the satellite gravimetry mission Gravity Recovery and Climate Experiment – Follow-On (GRACE-FO). However, the coarse spatial resolution of GRACE-FO may cause substantial signal leakage near the boundaries of the LRM zone, rendering local mass changes unreliable. To mitigate this, we instead investigate the entire EAIS sector and employ three basin-averaged Level-3 GRACE-FO products (Sasgen et al., 2019, 2020; Groh and Horwath, 2021). These products are derived from different Level-2 spherical harmonic solutions and incorporate distinct models for the glacial isostatic adjustment correction. Despite this broader approach, the GRACE-FO-based mass change estimates remain too uncertain to provide a robust validation, as their EAIS mass trends range from 106 to 156 $\mathrm{Gt\,yr^{-1}}$ for the period April 2019–October 2024. Furthermore, converting altimetry-derived volume changes to mass introduces additional uncertainty (Shepherd et al., 2012). This is why we test two conversion approaches: First, we apply a time-constant density model following Schröder et al. (2019). Second, we correct for changes in FAC to obtain ice-equivalent mass changes following Smith et al. (2020). Using our ICESat-2 trend estimate for the entire EAIS, including marginal regions, we derive mass trends of 106 and 155 $\mathrm{Gt\,yr^{-1}}$, respectively. Although the mass change estimates from satellite gravimetry and satellite altimetry fall within a similar range, the spread in their different solutions ($\approx 50\,\mathrm{Gt\,yr^{-1}}$) is too large to meaningfully evaluate the differences between ICESat-2 and CryoSat-2.

7 Conclusions

We analyse CryoSat-2 and ICESat-2 measurements to derive monthly gridded elevation changes for the CryoSat-2 Antarctic LRM zone - the relatively flat ice sheet interior, where topography-related errors play a minor role. By evaluating the radar and laser altimetry results and their differences for the 5.5-year period their data overlap (April 2019 to October 2024), we tackle the following three questions.

First, which of the radar-specific correction methods, particularly retracking and scattering corrections, yield the most accurate surface elevation change estimates when validated with ICESat-2? The choice of radar retracking algorithm is essential and affects the CryoSat-2 elevation change results in the entire study area. Within the group of conventional retrackers, the best CryoSat-2 result (i.e. most precise and accurate, smallest trend uncertainty and error) is given by OCOG10d. That uses a low-threshold retracker (10 % of the OCOG amplitude; Schröder et al., 2019) and correlates the elevation changes with BS and LEW variations based on monthly differences (Nilsson et al., 2022). For OCOG10, the application of a scattering correction is indispensable, with differences between scattering corrections being rather localised to certain regions. In total, the results of the AWI-ICENet1 convolutional neural network retracker (Helm et al., 2024) are best and surpass those of OCOG10d. For AWI-ICENet1, the application of a scattering correction loses importance.

Second, how consistent are CryoSat-2 and ICESat-2 elevation change trends across their 5.5-year period of overlap? We find systematic trend differences between ICESat-2 and CryoSat-2, which exist for any retracker and scattering correction, but are smallest with AWI-ICENet1. Yet, the trend derived from CryoSat-2 AWI-ICENet1c is 43 % less than the ICESat-2 trend

https://doi.org/10.5194/egusphere-2025-5745
Preprint. Discussion started: 15 December 2025

of $97 \pm 4\,\mathrm{km^3\,yr^{-1}}$. The thickening observed by ICESat-2 coincides with excess accumulation simulated by the GEMB model (Gardner et al., 2023) and appears systematically smaller for CryoSat-2. One of our hypotheses is that this might be because freshly fallen snow introduces stronger radar signal penetration. However, further work is needed to test this hypothesis, for example by incorporating more data sets from different sensors. In the regions where SMB and firn processes dominate the surface elevation trend, the systematic differences can be modelled by an offset of $0.2\,\mathrm{cm\,yr^{-1}}$ and a scale factor of 0.31 to the ICESat-2 trend. Apart from these systematic differences, the trend error (= ICESat-2−CryoSat-2 trend) is within the assessed standard uncertainty estimate.

Third, what level of certainty or accuracy can currently be achieved in determining elevation changes of the vast, low-relief AIS interior? For ICESat-2, we derive a mean trend uncertainty of $0.4 \pm 0.2\,\mathrm{cm\,yr^{-1}}$. We note that this estimate does not account for potential long-term drifts (Magruder et al., 2025), but does consider temporal correlations between monthly elevation changes, however these may be somewhat overestimated. The mean CryoSat-2 trend error is $0.6 \pm 1.0\,\mathrm{cm\,yr^{-1}}$ for AWI-ICENet1c (including the systematics), which primarily reflects errors related to radar signal penetration. For the whole grounded AIS, this could imply errors in the volume and mass trends of at least $74\,\mathrm{km^3\,yr^{-1}}$ and $28\,\mathrm{Gt\,yr^{-1}}$, respectively. These results emphasise the need for a comprehensive characterisation of uncertainties in altimetry results, and highlight the challenges of constraining small, long-term SMB-related trends by radar altimetry.

Code and data availability. The monthly gridded elevation changes from the ICESat-2 and CryoSat-2 altimetry data were largely generated using the "Cryosphere Altimetry Processing Toolkit" (captoolkit) available at https://github.com/nasa-jpl/captoolkit. ICESat-2 ATL06 data (Smith et al., 2023) can be downloaded at https://nsidc.org/data/ATL06/versions/6 (last access: 21 February 2025). CryoSat-2 Level-1B (ESA, 2023a) and Level-2I (ESA, 2023b) data can be downloaded at ftp://science-pds.cryosat.esa.int/ (last access: 20 December 2024). The outputs from the IMAU (Veldhuijsen et al., 2025) and GEMB (Schlegel and Gardner, 2025) firn models are available at https://zenodo.org/records/14634258 (last access: 24 April 2025) and https://zenodo.org/records/14714746 (last access: 20 February 2025), respectively. The ERA5 parameters (Hersbach et al., 2023) can be downloaded at https://cds.climate.copernicus.eu/datasets/reanalysis-era5-single-levels-monthly-means (last access: 7 February 2025). CryoSat-2 monthly gridded elevation change results from the AWI-ICENet1 retracker for the period 2011–2022 are published at https://doi.org/10.1594/PANGAEA.964596 (Helm, 2024). An updated version of the AWI-ICENet1 results and the results of this study, monthly gridded elevation changes from ICESat-2 and CryoSat-2 (for the OCOG10, OCOG30 and UCL-LI retrackers), will be available on PANGAEA.

Author contributions. Contributions are according to CRediT. Conceptualization: MTK, MH and JN. Formal analysis: MTK and VH. Funding acquisition: MH, VH and MTK. Methodology: MTK, JN and MH. Software: JN, MTK and ASG. Supervision: JN and MH. Visualization: MTK. Writing (majority of original draft): MTK. Writing (review and editing): JN, MH, VH and ASG.

Competing interests. The authors declare that they have no conflict of interest.

https://doi.org/10.5194/egusphere-2025-5745
Preprint. Discussion started: 15 December 2025

Acknowledgements. Maria T. Kappelsberger acknowledges founding by the Deutsche Forschungsgemeinschaft (DFG) as part of the Special Priority Programme (SPP) 1158 Antarctic Research with Comparative Investigations in Arctic Ice Areas (grant no. HO 4232/10-1, project no. 442929109) and by the Graduate Academy of Dresden University of Technology with funds from the Federal Government and the Federal State of Saxony. We acknowledge the computing time made available on the high-performance computer at the NHR (Nationales Hochleistungsrechnen) Center of TU Dresden. This center is jointly supported by the Federal Ministry of Education and Research and the state governments participating in the NHR (www.nhr-verein.de/unsere-partner). Our special thanks to the Jet Propulsion Laboratory (JPL) Visiting Student Research Program for facilitating Maria T. Kappelsberger's stay at JPL and thus initiating this work. We gratefully acknowledge the use of the algorithms of "captoolkit", the "Cryosphere Altimetry Processing Toolkit" (https://github.com/nasa-jpl/captoolkit). We thank the NASA and ESA for distributing their altimetry data.

https://doi.org/10.5194/egusphere-2025-5745
Preprint. Discussion started: 15 December 2025

References

Adusumilli, S., A. Fish, M., Fricker, H. A., and Medley, B.: Atmospheric River Precipitation Contributed to Rapid Increases in Surface Height of the West Antarctic Ice Sheet in 2019, Geophysical Research Letters, 48, e2020GL091 076, https://doi.org/10.1029/2020gl091076, 2021.

Amory, C., Buizert, C., Buzzard, S., Case, E., Clerx, N., Culberg, R., Datta, R., Dey, R., Drews, R., Dunmire, D., Eayrs, C., Hansen, N., Humbert, A., Kaitheri, A., Keegan, K., Kuipers Munneke, P., Lenaerts, J., Lhermitte, S., Mair, D., McDowell, I., Mejia, J., Meyer, C., Morris, E., Moser, D., Oraschewski, F., Pearce, E., de Roda Husman, S., Schlegel, N.-J., Schultz, T., Simonsen, S., Stevens, C., Thomas, E., Thompson-Munson, M., Wever, N., and Wouters, B.: Firn on ice sheets, Nature Reviews Earth & Environment, 5, 79–99, https://doi.org/10.1038/s43017-023-00507-9, 2024.

Andersen, O. B.: Cryo-TEMPO Product Handbook (ESA document LU_ESA_Cryo-TEMPO_PH), Tech. Rep. version 4.1, European Space Agency, https://earth.esa.int/eogateway/documents/d/earth-online/cryotempo-thematic-product-handbook-pdf, last access: 8 July 2025, 2025.

Armitage, T., Wingham, D., and Ridout, A.: Meteorological Origin of the Static Crossover Pattern Present in Low-Resolution-Mode CryoSat-2 Data Over Central Antarctica, IEEE Geosci. Remote Sens. Lett., 11, 1295–1299, https://doi.org/10.1109/LGRS.2013.2292821, 2014.

Arthern, R., Wingham, D., and Ridout, A.: Controls on ERS altimeter measurements over ice sheets: Footprint-scale topography, backscatter fluctuations, and the dependence of microwave penetration depth on satellite orientation, Journal of Geophysical Research: Atmospheres, 106, 33 471–33 484, https://doi.org/10.1029/2001JD000498, 2001.

Bae, S., Helgeson, B., James, M., Magruder, L., Sipps, J., Luthcke, S., and Thomas, T.: Performance of ICESat-2 Precision Pointing Determination, Earth and Space Science, 8, e2020EA001 478, https://doi.org/10.1029/2020EA001478, 2021.

Bamber, J.: Ice Sheet Altimeter Processing Scheme, International Journal of Remote Sensing, 15, 925–938, https://doi.org/10.1080/01431169408954125, 1994.

Blanchard-Wrigglesworth, E., Cox, T., Espinosa, Z., and Donohoe, A.: The Largest Ever Recorded Heatwave—Characteristics and Attribution of the Antarctic Heatwave of March 2022, Geophys. Res. Lett., 50, e2023GL104 910, https://doi.org/10.1029/2023GL104910, 2023.

Bos, M., Montillet, J.-P., Williams, S., and Fernandes, R.: Geodetic Time Series Analysis in Earth Sciences, chap. Introduction to Geodetic Time Series Analysis, pp. 29–52, Springer Geophysics, Springer International Publishing, Cham, Switzerland, ISBN 978-3-030-21718-1, https://doi.org/10.1007/978-3-030-21718-1_2, 2020.

Brown, G.: The average impulse response of a rough surface and its applications, IEEE Transactions on Antennas and Propagation, 25, 67–74, https://doi.org/10.1109/TAP.1977.1141536, 1977.

Brunt, K., Smith, B., Sutterley, T., Kurtz, N., and Neumann, T.: Comparisons of Satellite and Airborne Altimetry With Ground-Based Data From the Interior of the Antarctic Ice Sheet, Geophys. Res. Lett., 48, e2020GL090 572, https://doi.org/10.1029/2020GL090572, 2021.

Clem, K., Adusumilli, S., Baiman, R., Banwell, A., Barreira, S., Beadling, R., Bozkurt, D., Colwell, S., Coy, L., Datta, R., De Laat, J., du Plessis, M., Dunmire, D., Fogt, R., Freeman, N., Fricker, H., Gardner, A., Gille, S., Johnson, B., Josey, S., Keller, L., Kramarova, N., Lazzara, M., Lieser, J., MacFerrin, M., MacGilchrist, G., MacLennan, M., Massom, R., Mazloff, M., Mikolajczyk, D., Mote, T., Nash, E., Newman, P., Norton, T., Ochwat, N., Petropavlovskikh, I., Pezzi, L., Pitts, M., Raphael, M., Reid, P., Santee, M., Santini, M., Scambos, T., Schultz, C., Shi, J., Souza, E., Stammerjohn, S., Strahan, S., Thompson, A., Trusel, L., Wille, J., Yin, Z., Allen, J., Camper, A., Haley, B., Hammer, G., Love-Brotak, S., Ohlmann, L., Noguchi, L., Riddle, D., and Veasey, S.: Antarctica and the Southern Ocean, in:

https://doi.org/10.5194/egusphere-2025-5745
Preprint. Discussion started: 15 December 2025

State of the Climate in 2022, edited by Clem, K. and Raphael, M., pp. S322–S365, Bull. Amer. Meteor. Soc., 104(9), Boston MA, USA, https://doi.org/10.1175/BAMS-D-23-0077.1, 2023.

Davis, C.: A robust threshold retracking algorithm for measuring ice-sheet surface elevation change from satellite radar altimeters, Geoscience and Remote Sensing, IEEE Transactions on, 35, 974–979, https://doi.org/10.1109/36.602540, 1997.

Davis, C. and Ferguson, A.: Elevation change of the Antarctic ice sheet, 1995-2000, from ERS-2 satellite radar altimetry, IEEE Trans. Geosci. Remote Sens., 42, 2437–2445, https://doi.org/10.1109/TGRS.2004.836789, 2004.

Davison, B., Hogg, A., Rigby, R., Veldhuijsen, S., van Wessem, J., van den Broeke, M., Holland, P., Selley, H., and Dutrieux, P.: Sea level rise from West Antarctic mass loss significantly modified by large snowfall anomalies, Nature Communications, 14, 1479, https://doi.org/10.1038/s41467-023-36990-3, 2023.

Ekaykin, A., Veres, A., and Wang, Y.: Recent increase in the surface mass balance in central East Antarctica is unprecedented for the last 2000 years, Commun. Earth Environ., 5, 200, https://doi.org/10.1038/s43247-024-01355-1, 2024.

ESA: CryoSat-2 Product Handbook, Baseline E 1.0 - Draft C (ESA document C2-LI-ACS-ESL-5319), Tech. rep., European Space Agency, https://earth.esa.int/eogateway/documents/20142/0/CryoSat-Product-Handbook-Baseline-E-draft.pdf, last access: 13 September 2025, 2021.

ESA: L1b LRM Precise Orbit, Baseline E [dataset], European Space Agency, https://doi.org/10.5270/CR2-41ad749, last access: 20 December 2024, 2023a.

ESA: L2 LRM Precise Orbit. Baseline E [dataset], European Space Agency, https://doi.org/10.5270/CR2-614f341, last access: 20 December 2024, 2023b.

Ferguson, A., Davis, C., and Cavanaugh, J.: An autoregressive model for analysis of ice sheet elevation change time series, IEEE Transactions on Geoscience and Remote Sensing, 42, 2426–2436, https://doi.org/10.1109/TGRS.2004.836788, 2004.

Flament, T. and Rémy, F.: Dynamic thinning of Antarctic glaciers from along-track repeat radar altimetry, Journal of Glaciology, 58, 830–840, https://doi.org/10.3189/2012JoG11J118, 2012.

Fricker, H. A., Galton-Fenzi, B. K., Walker, C. C., Freer, B. I. D., Padman, L., and DeConto, R.: Antarctica in 2025: Drivers of deep uncertainty in projected ice loss, Science, 387, 601–609, https://doi.org/10.1126/science.adt9619, 2025.

Gardner, A., Moholdt, G., Scambos, T., Fahnstock, M., Ligtenberg, S., van den Broeke, M., and Nilsson, J.: Increased West Antarctic and unchanged East Antarctic ice discharge over the last 7 years, The Cryosphere, 12, 521–547, https://doi.org/10.5194/tc-12-521-2018, 2018.

Gardner, A., Schlegel, N.-J., and Larour, E.: Glacier Energy and Mass Balance (GEMB): a model of firn processes for cryosphere research, Geoscientific Model Development, 16, 2277–2302, https://doi.org/10.5194/gmd-16-2277-2023, 2023.

Groh, A. and Horwath, M.: Antarctic Ice Mass Change Products from GRACE/GRACE-FO Using Tailored Sensitivity Kernels, Remote Sensing, 13, https://doi.org/10.3390/rs13091736, 2021.

Hai, G., Cheng, Y., Xie, H., Hao, T., Qiao, G., and Li, R.: Assessment of CryoSat-2 Baseline-D Height Product by GNSS and ICESat-2 in Lambert-Amery System, East Antarctica, IEEE Journal of Selected Topics in Applied Earth Observations and Remote Sensing, 15, 2891–2900, https://doi.org/10.1109/JSTARS.2022.3156929, 2022.

Hanna, E., Topál, D., Box, J., Buzzard, S., Christie, F., Hvidberg, C., Morlighem, M., De Santis, L., Silvano, A., Colleoni, F., Sasgen, I., Banwell, A., van den Broeke, M., DeConto, R., De Rydt, J., Goelzer, H., Gossart, A., Gudmundsson, G., Lindbäck, K., Miles, B., Mottram, R., Pattyn, F., Reese, R., Rignot, E., Srivastava, A., Sun, S., Toller, J., Tuckett, P., and Ultee, L.: Short- and long-term variability of the Antarctic and Greenland ice sheets, Nature Reviews Earth & Environment, 5, 193–210, https://doi.org/10.1038/s43017-023-00509-7, 2024.

https://doi.org/10.5194/egusphere-2025-5745
Preprint. Discussion started: 15 December 2025

Helm, V.: Convolutional neural network training dataset and results of AWI-ICENet1 retracker [dataset], PANGAEA, https://doi.org/10.1594/PANGAEA.964596, 2024.

Helm, V., Humbert, A., and Miller, H.: Elevation and elevation change of Greenland and Antarctica derived from CryoSat-2, The Cryosphere, 8, 1539–1559, https://doi.org/10.5194/tc-8-1539-2014, 2014.

Helm, V., Dehghanpour, A., Hänsch, R., Loebel, E., Horwath, M., and Humbert, A.: AWI-ICENet1: a convolutional neural network retracker for ice altimetry, The Cryosphere, 18, 3933–3970, https://doi.org/10.5194/tc-18-3933-2024, 2024.

Hersbach, H., Bell, B., Berrisford, P., Hirahara, S., Horányi, A., Muñoz-Sabater, J., Nicolas, J., Peubey, C., Radu, R., Schepers, D., Simmons, A., Soci, C., Abdalla, S., Abellan, X., Balsamo, G., Bechtold, P., Biavati, G., Bidlot, J., Bonavita, M., De Chiara, G., Dahlgren, P., Dee, D., Diamantakis, M., Dragani, R., Flemming, J., Forbes, R., Fuentes, M., Geer, A., Haimberger, L., Healy, S., Hogan, R., Hólm, E., Janisková, M., Keeley, S., Laloyaux, P., Lopez, P., Lupu, C., Radnoti, G., de Rosnay, P., Rozum, I., Vamborg, F., Villaume, S., and Thépaut, J.-N.: The ERA5 global reanalysis, Quart. J. R. Met. Soc., 146, 1999–2049, https://doi.org/10.1002/qj.3803, 2020.

Hersbach, H., Bell, B., Berrisford, P., Biavati, G., Horányi, A., Muñoz Sabater, J., Nicolas, J., Peubey, C., Radu, R., Rozum, I., Schepers, D., Simmons, A., Soci, C., Dee, D., and Thépaut, J.-N.: ERA5 monthly averaged data on single levels from 1940 to present [dataset], Copernicus Climate Change Service (C3S) Climate Data Store (CDS), https://doi.org/10.24381/cds.f17050d7, last access: 7 February 2025, 2023.

Howat, I., Porter, C., Smith, B., Noh, M.-J., and Morin, P.: The Reference Elevation Model of Antarctica, The Cryosphere, 13, https://doi.org/10.5194/tc-13-665-2019, 2019.

Howat, I., Porter, C., Noh, M.-J., Husby, E., Khuvis, S., Danish, E., Tomko, K., Gardiner, J., Negrete, A., Yadav, B., Klassen, J., Kelleher, C., Cloutier, M., Bakker, J., Enos, J., Arnold, G., Bauer, G., and Morin, P.: The Reference Elevation Model of Antarctica – Mosaics, Version 2 [dataset], Harvard Dataverse, V1, https://doi.org/10.7910/DVN/EBW8UC, last access: 25 August 2022, 2022.

Kappelsberger, M. T., Horwath, M., Buchta, E., Willen, M. O., Schröder, L., Veldhuijsen, S. B. M., Kuipers Munneke, P., and van den Broeke, M. R.: How well can satellite altimetry and firn models resolve Antarctic firn thickness variations?, The Cryosphere, 18, 4355–4378, https://doi.org/10.5194/tc-18-4355-2024, 2024.

Khvorostovsky, K.: Merging and Analysis of Elevation Time Series Over Greenland Ice Sheet From Satellite Radar Altimetry, IEEE Trans. Geosci. Remote Sens., 50, 23–36, https://doi.org/10.1109/TGRS.2011.2160071, 2012.

King, M. and Christoffersen, P.: Major Modes of Climate Variability Dominate Nonlinear Antarctic Ice-Sheet Elevation Changes 2002–2020, Geophysical Research Letters, 51, e2024GL108 844, https://doi.org/10.1029/2024gl108844, 2024.

King, M. and Watson, C.: Antarctic Surface Mass Balance: Natural Variability, Noise, and Detecting New Trends, Geophys. Res. Lett., 47, e2020GL087 493, https://doi.org/10.1029/2020GL087493, 2020.

Kittel, C., Amory, C., Agosta, C., Jourdain, N. C., Hofer, S., Delhasse, A., Doutreloup, S., Huot, P.-V., Lang, C., Fichefet, T., and Fettweis, X.: Diverging future surface mass balance between the Antarctic ice shelves and grounded ice sheet, The Cryosphere, 15, 1215–1236, https://doi.org/10.5194/tc-15-1215-2021, 2021.

Koch, K.: Parameter Estimation and Hypothesis Testing in Linear Models, Springer Berlin, Heidelberg, 2 edn., https://doi.org/10.1007/978-3-662-03976-2, 1999.

Krieger, L., Strößenreuther, U., Helm, V., Floricioiu, D., and Horwath, M.: Synergistic Use of Single-Pass Interferometry and Radar Altimetry to Measure Mass Loss of NEGIS Outlet Glaciers between 2011 and 2014, Remote Sens., 12, 996, https://doi.org/10.3390/rs12060996, 2020.

https://doi.org/10.5194/egusphere-2025-5745
Preprint. Discussion started: 15 December 2025

Larue, F., Picard, G., Aublanc, J., Arnaud, L., Robledano-Perez, A., LE Meur, E., Favier, V., Jourdain, B., Savarino, J., and Thibaut, P.: Radar altimeter waveform simulations in Antarctica with the Snow Microwave Radiative Transfer Model (SMRT), Remote Sens. Environ., 263, 112 534, https://doi.org/10.1016/j.rse.2021.112534, 2021.

Legrésy, B. and Rémy, F.: Altimetric observations of surface characteristics of the Antarctic ice sheet, Journal of Glaciology, 43, 265–275, https://doi.org/10.3189/S002214300000321X, 1997.

Legrésy, B. and Rémy, F.: Using the temporal variability of satellite radar altimetric observation to map surface properties of the Antarctic ice sheet, Journal of Glaciology, 44, 207–213, https://doi.org/10.3189/S0022143000002537, 1998.

Legresy, B., Remy, F., and Schaeffer, P.: Different ERS altimeter measurements between ascending and descending tracks caused by wind induced features over ice sheets, Geophysical Research Letters, 26, 2231–2234, https://doi.org/https://doi.org/10.1029/1999GL900531, 1999.

Legrésy, B., Papa, F., Rémy, F., Vinay, G., van den Bosch, M., and Zanife, O.-Z.: ENVISAT radar altimeter measurements over continental surfaces and ice caps using the ICE-2 retracking algorithm, Remote Sens. Environ., 95, 150–163, https://doi.org/10.1016/j.rse.2004.11.018, 2005.

Li, S., Liao, J., and Zhang, L.: Extraction and analysis of elevation changes in Antarctic ice sheet from CryoSat-2 and Sentinel-3 radar altimeters, Journal of Applied Remote Sensing, 16, 034 514, https://doi.org/10.1117/1.JRS.16.034514, 2022.

Li, Y. and Davis, C.: Decadal Mass Balance of the Greenland and Antarctic Ice Sheets from High Resolution Elevation Change Analysis of ERS-2 and Envisat Radar Altimetry Measurements, in: IGARSS 2008 - 2008 IEEE International Geoscience and Remote Sensing Symposium, vol. 4, pp. IV–339–IV–342, https://doi.org/10.1109/IGARSS.2008.4779727, 2008.

Luthcke, S., Thomas, T., Pennington, T., Rebold, T., Nicholas, J., Rowlands, D., Gardner, A., and Bae, S.: ICESat-2 Pointing Calibration and Geolocation Performance, Earth and Space Science, 8, e2020EA001 494, https://doi.org/10.1029/2020EA001494, 2021.

Magruder, L., Brunt, K., Neumann, T., Klotz, B., and Alonzo, M.: Passive Ground-Based Optical Techniques for Monitoring the On-Orbit ICESat-2 Altimeter Geolocation and Footprint Diameter, Earth and Space Science, 8, e2020EA001 414, https://doi.org/10.1029/2020EA001414, 2021.

Magruder, L., Neumann, T., Kurtz, N., Sutterley, T., Hancock, D., Vornberger, P., Robbins, J., and Smith, B.: Assessment of the Ice, Cloud, and Land Elevation Satellite-2 Performance Against Prime Mission Science Requirements, Earth and Space Science, 12, e2025EA004 221, https://doi.org/10.1029/2025EA004221, 2025.

Markus, T., Neumann, T., Martino, A., Abdalati, W., Brunt, K., Csatho, B., Farrell, S., Fricker, H., Gardner, A., Harding, D., Jasinski, M., Kwok, R., Magruder, L., Lubin, D., Luthcke, S., Morison, J., Nelson, R., Neuenschwander, A., Palm, S., Popescu, S., Shum, C., Schutz, B., Smith, B., Yang, Y., and Zwally, H.: The Ice, Cloud, and land Elevation Satellite-2 (ICESat-2): Science requirements, concept, and implementation, Remote Sens. Environ., 190, 260–273, https://doi.org/10.1016/j.rse.2016.12.029, 2017.

McMillan, M., Shepherd, A., Sundal, A., Briggs, K., Muir, A., Ridout, A., Hogg, A., and Wingham, D.: Increased ice losses from Antarctica detected by CryoSat-2, Geophys. Res. Lett., 41, 3899–3905, https://doi.org/10.1002/2014GL060111, 2014.

Muir, A.: Cryo-TEMPO Algorithm Theoretical Basis Document Land Ice (ESA document LU_ESA_Cryo-TEMPO_ATBD_LI), Tech. Rep. version 4.2, European Space Agency, https://earth.esa.int/eogateway/documents/d/earth-online/cryo-tempo-atbd-land-ice, last access: 8 July 2025, 2024.

Neumann, T., A., B., Hancock, D., Robbins, J., Gibbons, A., Lee, J., Harbeck, K., Saba, J., Luthcke, S., and Rebold, T.: Ice, Cloud, and Land Elevation Satellite (ICESat-2) Project Algorithm Theoretical Basis Document (ATBD) for Global Geolocated Photons ATL03, Version 6, Tech. rep., NASA Goddard Space Flight Center, Greenbelt, Maryland, https://doi.org/10.5067/GA5KCLJT7LOT, 2022.

https://doi.org/10.5194/egusphere-2025-5745
Preprint. Discussion started: 15 December 2025

Nicola, L., Notz, D., and Winkelmann, R.: Revisiting temperature sensitivity: how does Antarctic precipitation change with temperature?, The Cryosphere, 17, 2563–2583, https://doi.org/10.5194/tc-17-2563-2023, 2023.

Nield, G. A., Whitehouse, P. L., King, M. A., and Clarke, P. J.: Glacial isostatic adjustment in response to changing Late Holocene behaviour of ice streams on the Siple Coast, West Antarctica, Geophysical Journal International, 205, 1–21, https://doi.org/10.1093/gji/ggv532, 2016.

Nilsson, J., Vallelonga, P., Simonsen, S., Sørensen, L., Forsberg, R., Dahl-Jensen, D., Hirabayashi, M., Goto-Azuma, K., Hvidberg, C., Kjaer, H., and Satow, K.: Greenland 2012 melt event effects on CryoSat-2 radar altimetry, Geophys. Res. Lett., 42, 3919–3926, https://doi.org/10.1002/2015GL063296, 2015.

Nilsson, J., Gardner, A., and Paolo, F.: Elevation change of the Antarctic Ice Sheet: 1985 to 2020, Earth System Science Data, 14, 3573–3598, https://doi.org/10.5194/essd-14-3573-2022, 2022.

Otosaka, I., Shepherd, A., and McMillan, M.: Ice Sheet Elevation Change in West Antarctica from Ka-band Satellite Radar Altimetry, Geophysical Research Letters, 46, https://doi.org/10.1029/2019GL084271, 2019.

Otosaka, I., Horwath, M., Mottram, R., and Nowicki, S.: Mass Balances of the Antarctic and Greenland Ice Sheets Monitored from Space, Surv. Geophys., 44, 1615–1652, https://doi.org/10.1007/s10712-023-09795-8, 2023a.

Otosaka, I., Shepherd, A., Ivins, E., Schlegel, N.-J., Amory, C., van den Broeke, M., Horwath, M., Joughin, I., King, M., Krinner, G., Nowicki, S., Payne, A., Rignot, E., Scambos, T., Simon, K., Smith, B., Sørensen, L., Velicogna, I., Whitehouse, P., A, G., Agosta, C., Ahlstrøm, A., Blazquez, A., Colgan, W., Engdahl, M., Fettweis, X., Forsberg, R., Gallée, H., Gardner, A., Gilbert, L., Gourmelen, N., Groh, A., Gunter, B., Harig, C., Helm, V., Khan, S., Kittel, C., Konrad, H., Langen, P., Lecavalier, B., Liang, C.-C., Loomis, B., McMillan, M., Melini, D., Mernild, S., Mottram, R., Mouginot, J., Nilsson, J., Noël, B., Pattle, M., Peltier, W., Pie, N., Roca, M., Sasgen, I., Save, H., Seo, K.-W., Scheuchl, B., Schrama, E., Schröder, L., Simonsen, S., Slater, T., Spada, G., Sutterley, T., Vishwakarma, B., van Wessem, J., Wiese, D., van der Wal, W., and Wouters, B.: Mass balance of the Greenland and Antarctic ice sheets from 1992 to 2020, Earth System Science Data, 15, 1597–1616, https://doi.org/10.5194/essd-15-1597-2023, 2023b.

Popov, S. and Chernoglazov, Y.: Vostok Subglacial Lake, East Antarctica: Lake shoreline and subglacial water caves [in Russian, with English summary], Ice and Snow, 1 (113), 12–24, 2011.

Ravinder, N., Shepherd, A., Otosaka, I., Slater, T., Muir, A., and Gilbert, L.: Greenland Ice Sheet Elevation Change From CryoSat-2 and ICESat-2, Geophysical Research Letters, 51, e2024GL110 822, https://doi.org/10.1029/2024gl110822, 2024.

Remy, F., Legresy, B., and Benveniste, J.: On the Azimuthally Anisotropy Effects of Polarization for Altimetric Measurements, IEEE Transactions on Geoscience and Remote Sensing, 44, 3289–3296, https://doi.org/10.1109/TGRS.2006.878444, 2006.

Rémy, F., Flament, T., Blarel, F., and Benveniste, J.: Radar altimetry measurements over antarctic ice sheet: A focus on antenna polarization and change in backscatter problems, Adv. Space Res., 50, 998–1006, https://doi.org/10.1016/j.asr.2012.04.003, 2012.

Ridley, J. and Partington, K.: A model of satellite radar altimeter return from ice sheets, Int. J. Remote Sensing, 9, 601–624, https://doi.org/10.1080/01431168808954881, 1988.

Rignot, E., Mouginot, J., and Scheuchl, B.: Ice Flow of the Antarctic Ice Sheet, Science, 333, https://doi.org/10.1126/science.1208336, 2011a.

Rignot, E., Mouginot, J., and Scheuchl, B.: Antarctic grounding line mapping from differential satellite radar interferometry, Geophysical Research Letters, 38, https://doi.org/10.1029/2011GL047109, 2011b.

Rignot, E., Mouginot, J., Scheuchl, B., van den Broeke, M., Van Wessem, J., and Morlighem, M.: Four decades of Antarctic Ice Sheet mass balance from 1979–2017, Proc. Natl. Acad. Sci. USA, 116, 1095–1103, https://doi.org/10.1073/pnas.1812883116, 2019.

https://doi.org/10.5194/egusphere-2025-5745
Preprint. Discussion started: 15 December 2025

Roemer, S., Legrésy, B., Horwath, M., and Dietrich, R.: Refined analysis of radar altimetry data applied to the region of the subglacial Lake Vostok / Antarctica, Remote Sens. Environ., 106, 269–284, https://doi.org/10.1016/j.rse.2006.02.026, 2007.

Ronan, A. C., Hawley, R. L., and Chipman, J. W.: Impacts of differing melt regimes on satellite radar waveforms and elevation retrievals, The Cryosphere, 18, 5673–5683, https://doi.org/10.5194/tc-18-5673-2024, 2024.

Sandberg Sørensen, L., Simonsen, S., Forsberg, R., Khvorostovsky, K., Meister, R., and Engdahl, M.: 25 years of elevation changes of the Greenland Ice Sheet from ERS, Envisat, and CryoSat-2 radar altimetry, Earth Planet. Sci. Lett., 495, 234–241, https://doi.org/10.1016/j.epsl.2018.05.015, 2018.

Sasgen, I., Groh, A., and Horwath, M.: GFZ GravIS RL06 Ice-Mass Change Products. V. 0004 [dataset], GFZ Data Services, https://doi.org/10.5880/GFZ.GRAVIS_06_L3_ICE, last access: 15 September 2025, 2019.

Sasgen, I., Groh, A., and Horwath, M.: COST-G GravIS RL01 Ice-Mass Change Products. V. 0003 [dataset], GFZ Data Services, https://doi.org/10.5880/COST-G.GRAVIS_01_L3_ICE, last access: 15 September 2025, 2020.

Schlegel, N.-J. and Gardner, A.: Output from the Glacier Energy and Mass Balance (GEMB v1.0) forced with 3-hourly ERA5 fields and gridded to 10km, Greenland and Antarctica 1979-2024 (version 1.4) [dataset], Zenodo, https://doi.org/10.5281/zenodo.14714746, last access: 20 February 2025, 2025.

Schröder, L., Richter, A., Fedorov, D., Eberlein, L., Brovkov, E., Popov, S., Knöfel, C., Horwath, M., Dietrich, R., Matveev, A., Scheinert, M., and Lukin, V.: Validation of satellite altimetry by kinematic GNSS in central East Antarctica, The Cryosphere, 11, 1111–1130, https://doi.org/10.5194/tc-11-1111-2017, 2017.

Schröder, L., Horwath, M., Dietrich, R., Helm, V., van den Broeke, M., and Ligtenberg, S.: Four decades of Antarctic surface elevation changes from multi-mission satellite altimetry, The Cryosphere, 13, 427–449, https://doi.org/10.5194/tc-13-427-2019, 2019.

Shepherd, A., Ivins, E., A, G., Barletta, V., Bentley, M., Bettadpur, S., Briggs, K., Bromwich, D., Forsberg, R., Galin, N., Horwath, M., Jacobs, S., Joughin, I., King, M., Lenaerts, J., Li, J., Ligtenberg, S., Luckman, A., Luthcke, S., McMillan, M., Meister, R., Milne, G., Mouginot, J., Muir, A., Nicolas, J., Paden, J., Payne, A., Pritchard, H., Rignot, E., Rott, H., Sorensen, L., Scambos, T., Scheuchl, B., Schrama, E., Smith, B., Sundal, A., van Angelen, J., van de Berg, W., van den Broeke, M., Vaughan, D., Velicogna, I., Wahr, J., Whitehouse, P., Wingham, D., Yi, D., Young, D., and Zwally, H.: A Reconciled Estimate of Ice-Sheet Mass Balance, Science, 338, https://doi.org/10.1126/science.1228102, 2012.

Shepherd, A., Gilbert, L., Muir, A., Konrad, H., McMillan, M., Slater, T., Briggs, K., Sundal, A., Hogg, A., and Engdahl, M.: Trends in Antarctic Ice Sheet Elevation and Mass, Geophys. Res. Lett., 46, 8174–8183, https://doi.org/10.1029/2019GL082182, 2019.

Simonsen, S. and Sørensen, L.: Implications of changing scattering properties on Greenland ice sheet volume change from Cryosat-2 altimetry, Remote Sens. Environ., 190, 207–216, https://doi.org/10.1016/j.rse.2016.12.012, 2017.

Slater, T., Shepherd, A., McMillan, M., Muir, A., Gilbert, L., Hogg, A. E., Konrad, H., and Parrinello, T.: A new digital elevation model of Antarctica derived from CryoSat-2 altimetry, The Cryosphere, 12, 1551–1562, https://doi.org/10.5194/tc-12-1551-2018, 2018.

Smith, B., Fricker, H., Holschuh, N., Gardner, A., Adusumilli, S., Brunt, K., Csatho, B., Harbeck, K., Huth, A., Neumann, T., Nilsson, J., and Siegfried, M.: Land ice height-retrieval algorithm for NASA's ICESat-2 photon-counting laser altimeter, Remote Sens. Environ., 233, 111 352, https://doi.org/10.1016/j.rse.2019.111352, 2019.

Smith, B., Fricker, H. A., Gardner, A. S., Medley, B., Nilsson, J., Paolo, F. S., Holschuh, N., Adusumilli, S., Brunt, K., Csatho, B., Harbeck, K., Markus, T., Neumann, T., Siegfried, M. R., and Zwally, H.: Pervasive ice sheet mass loss reflects competing ocean and atmosphere processes, Science, https://doi.org/10.1126/science.aaz5845, 2020.

https://doi.org/10.5194/egusphere-2025-5745
Preprint. Discussion started: 15 December 2025

Smith, B., Adusumilli, S., Csathó, B., Felikson, D., Fricker, H., Gardner, A., Holschuh, N., Lee, J., Nilsson, J., Paolo, F., Siegfried, M., Sutterley, T., and the ICESat-2 Science Team: ATLAS/ICESat-2 L3A Land Ice Height (ATL06, Version 6) [dataset], NASA National Snow and Ice Data Center Distributed Active Archive Center, https://doi.org/10.5067/ATLAS/ATL06.006, last access: 21 February 20, 2023.

Sørensen, L., Simonsen, S., Meister, R., Forsberg, R., Levinsen, J., and Flament, T.: Envisat-derived elevation changes of the Greenland ice sheet, and a comparison with ICESat results in the accumulation area, Remote Sens. Environ., 160, 56–62, https://doi.org/10.1016/j.rse.2014.12.022, 2015.

Stokes, C., Abram, N., Bentley, M., Edwards, T., England, M., Foppert, A., Jamieson, S., Jones, R., King, M., Lenaerts, J., Medley, B., Miles, B., Paxman, G., Ritz, C., van de Flierdt, T., and Whitehouse, P.: Response of the East Antarctic Ice Sheet to past and future climate change, Nature, 608, 275–286, https://doi.org/10.1038/s41586-022-04946-0, 2022.

Studinger, M., Smith, B. E., Kurtz, N., Petty, A., Sutterley, T., and Tilling, R.: Estimating differential penetration of green (532 nm) laser light over sea ice with NASA's Airborne Topographic Mapper: observations and models, The Cryosphere, 18, 2625–2652, https://doi.org/10.5194/tc-18-2625-2024, 2024.

Veldhuijsen, S., van de Berg, W., Brils, M., Kuipers Munneke, P., and van den Broeke, M.: Characteristics of the 1979–2020 Antarctic firn layer simulated with IMAU-FDM v1.2A, The Cryosphere, 17, 1675–1696, https://doi.org/10.5194/tc-17-1675-2023, 2023.

Veldhuijsen, S., van de Berg, W., van den Broeke, M., and Kuipers Munneke, P.: IMAU-FDM v1.2A variables over Antarctica (1979-2023) [dataset], Zenodo, https://doi.org/10.5281/zenodo.14634258, last access: 24 April 2025, 2025.

Verron, J., Sengenes, P., Lambin, J., Noubel, J., Steunou, N., Guillot, A., Picot, N., Coutin-Faye, S., Sharma, R., Gairola, R., Murthy, D., Richman, J., Griffin, D., Pascual, A., Rémy, F., and Gupta, P.: The SARAL/AltiKa Altimetry Satellite Mission, Marine Geodesy, 38, https://doi.org/10.1080/01490419.2014.1000471, 2015.

Wang, S., Liu, J., Cai, W., Yang, D., Kerzenmacher, T., Ding, S., and Cheng, X.: Strong impact of the rare three-year La Niña event on Antarctic surface climate changes in 2021–2023, npj Climate and Atmospheric Science, 8, 173, https://doi.org/10.1038/s41612-025-01066-0, 2025.

Wang, Y., Wu, Q., Zhang, X., and Zhai, Z.: Record-breaking Antarctic snowfall in 2022 delays global sea level rise, Science Bulletin, 68, 3154–3157, https://doi.org/10.1016/j.scib.2023.08.055, 2023.

Wille, J., Alexander, S., Amory, C., Baiman, R., Barthélemy, L., Bergstrom, D., Berne, A., Binder, H., Blanchet, J., Bozkurt, D., Bracegirdle, T., Casado, M., Choi, T., Clem, K., Codron, F., Datta, R., Battista, S., Favier, V., Francis, D., Fraser, A., Fourré, E., Garreaud, R., Genthon, C., Gorodetskaya, I., González-Herrero, S., Heinrich, V., Hubert, G., Joos, H., Kim, S., King, J., Kittel, C., Landais, A., Lazzara, M., Leonard, G., Lieser, J., Maclennan, M., Mikolajczyk, D., Neff, P., Ollivier, I., Picard, G., Pohl, B., Ralph, F., Rowe, P., Schlosser, E., Shields, C., Smith, I., Sprenger, M., Trusel, L., Udy, D., Vance, T., Vignon, É., Walker, C., Wever, N., and Zou, X.: The Extraordinary March 2022 East Antarctica ''Heat'' Wave. Part II: Impacts on the Antarctic Ice Sheet, Journal of Climate, 37, 779–799, https://doi.org/10.1175/JCLI-D-23-0176.1, 2024a.

Wille, J., Alexander, S., Amory, C., Baiman, R., Barthélemy, L., Bergstrom, D., Berne, A., Binder, H., Blanchet, J., Bozkurt, D., Bracegirdle, T., Casado, M., Choi, T., Clem, K., Codron, F., Datta, R., Di Battista, S., Favier, V., Francis, D., Fraser, A., Fourré, E., Garreaud, R., Genthon, C., Gorodetskaya, I., González-Herrero, S., Heinrich, V., Hubert, G., Joos, H., Kim, S., King, J., Kittel, C., Landais, A., Lazzara, M., Leonard, G., Lieser, J., Maclennan, M., Mikolajczyk, D., Neff, P., Ollivier, I., Picard, G., Pohl, B., Ralph, F., Rowe, P., Schlosser, E., Shields, C., Smith, I., Sprenger, M., Trusel, L., Udy, D., Vance, T., Vignon, É., Walker, C., Wever, N., and Zou, X.: The Extraor-

https://doi.org/10.5194/egusphere-2025-5745
Preprint. Discussion started: 15 December 2025

dinary March 2022 East Antarctica ‘‘Heat’’ Wave. Part I: Observations and Meteorological Drivers, Journal of Climate, 37, 757–778, https://doi.org/10.1175/JCLI-D-23-0175.1, 2024b.

Wingham, D., Rapley, C., and Griffiths, H.: New techniques in satellite altimeter tracking systems, in: ESA Proceedings of the 1986 International Geoscience and Remote Sensing Symposium(IGARSS'86) on Remote Sensing: Today's Solutions for Tomorrow's Information Needs, vol. 3, pp. 1339–1344, https://www.researchgate.net/publication/269518510, 1986.

Wingham, D., Ridout, A., Scharroo, R., Arthern, R., and Shum, C.: Antarctic Elevation Change from 1992 to 1996, Science, 282, 456–458, https://doi.org/10.1126/science.282.5388.456, 1998.

Wingham, D., Francis, C., Baker, S., Bouzinac, C., Brockley, D., Cullen, R., Chateau-Thierry, P. d., Laxon, S., Mallow, U., Mavrocordatos, C., Phalippou, L., Ratier, G., Rey, L., Rostan, F., Viau, P., and Wallis, D.: CryoSat: A mission to determine the fluctuations in Earth's land and marine ice fields, Adv. Space Res., 37, 841–871, https://doi.org/10.1016/j.asr.2005.07.027, 2006.

Yue, L., Chao, N., Chen, G., Chen, L., Zhang, B., Sun, R., Zhang, Y., Wang, S., Wang, Z., Li, F., Yu, N., and Ouyang, G.: Reconstructing Continuous Ice Sheet Elevation Changes in the Amundsen Sea Sector During 2003–2021 by Merging Envisat, ICESat, CryoSat-2, and ICESat-2 Multi-Altimeter Observations, Journal of Geophysical Research: Earth Surface, 128, e2022JF007 020, https://doi.org/10.1029/2022jf007020, 2023.

Zhai, Z., Wang, Y., Wu, Q., and Hou, S.: Record-Breaking Warm Late-Winter Over Antarctica in 2024: The Role of Western Pacific Warm Pool and Pacific Decadal Oscillation, Geophysical Research Letters, 52, e2024GL114 528, https://doi.org/10.1029/2024gl114528, 2025.

Zhang, B., Wang, Z., Yang, Q., Liu, J., An, J., Li, F., Liu, T., and Geng, H.: Elevation Changes of the Antarctic Ice Sheet from Joint Envisat and CryoSat-2 Radar Altimetry, Remote Sensing, 12, https://doi.org/10.3390/rs12223746, 2020.